

Dependence of Polar Low Development on Baroclinicity and Physical Processes: An Idealized High-Resolution Numerical Experiment

WATARU YANASE* AND HIROSHI NIINO

Ocean Research Institute, University of Tokyo, Tokyo, Japan

(Manuscript received 25 January 2006, in final form 23 October 2006)

ABSTRACT

Polar low dynamics in an idealized atmosphere in which baroclinicity, stratification, and average temperature are varied in the typically observed range is investigated using a 5-km-resolution nonhydrostatic model. The baroclinicity is found to be the most important factor that strongly controls the polar low dynamics.

When the baroclinicity is weak, a small, nearly axisymmetric vortex develops through a cooperative interaction between the vortex flow and cumulus convection. The surface friction promotes the vortex dynamics by transporting the sensible heat and moisture into the vortex center. The vortex development has a strong sensitivity to the initial perturbation.

As the baroclinicity is increased, most of the characteristics of polar low dynamics change smoothly without showing any significant regime shift. The vortex for an intermediate baroclinicity, however, moves northward, which is a unique behavior. This is caused by vortex stretching on the northern side of the vortex where intense convection produces a stronger updraft.

When the baroclinicity is strong, a larger vortex with a comma-shaped cloud pattern develops. The condensational heating, baroclinic conversion from the basic available potential energy, and conversion from the basic kinetic energy through the vertical shear all contribute to the vortex development, which depends little on the initial perturbation. The above relations between baroclinicity and vortex dynamics are proved to be robust in the typically observed range of stratification and average temperature.

1. Introduction

Polar lows are mesoscale cyclones that develop over high-latitude oceans on the polar side of the polar front in cold seasons (Harley 1960; Businger and Reed 1989; Heinemann and Claud 1997; Rasmussen and Turner 2003). Their horizontal scale ranges from 200 to 1000 km and the maximum wind speed exceeds 15 m s^{-1} . A number of meteorologists have been interested in the structure and dynamics of polar lows not only because they cause hazardous weather but also because they exhibit a wide variety of cloud patterns (Carleton 1985; Forbes and Lottes 1985; Heinemann 1990): some of them resemble tropical cyclones having a cloud-free

eye and spiral cloud bands (e.g., Businger and Baik 1991; Nordeng and Rasmussen 1992), some look like miniature extratropical cyclones having a comma-shaped cloud pattern (e.g., Reed and Duncan 1987), and the others have complicated cloud patterns (e.g., Rasmussen 1981, 1985). However, it is not easy to observe their detailed structures because they are small short-lived cyclones that form over the data-sparse high-latitude oceans in winter.

Since the early studies on polar lows, several mechanisms for the development of polar lows have been suggested (e.g., Rasmussen and Turner 2003). One candidate is an instability due to diabatic processes such as condensational heating and sea surface heat fluxes; for example, the conditional instability of the second kind (CISK) mechanism suggested by Bratseth (1985) and Rasmussen (1985), and the wind-induced surface heat exchange (WISHE) by Emanuel and Rotunno (1989), which were originally suggested to explain the development of the tropical cyclone. Satellite observations consistently show active cumulus convection within polar lows (Businger and Baik 1991; Nordeng and Ras-

* Current affiliation: Center for Climate System Research, University of Tokyo, Chiba, Japan.

Corresponding author address: Wataru Yanase, Center for Climate System Research, University of Tokyo, 5-1-5, Kashiwanoha, Kashiwa, Chiba 277-8568, Japan.
E-mail: yanase@ccsr.utokyo.ac.jp

mussen 1992). Linear analyses (Rasmussen 1979; Økland 1987) have been performed to understand the growth rate and horizontal scale of the polar low that develop through the diabatic processes. Another candidate is a baroclinic instability within a shallow regional-scale temperature contrast between the air over a cold land surface (or sea ice) and that over a relatively warm sea surface (Reed and Duncan 1987; Tsuboki and Wakahama 1992). Harrold and Browning (1969) reported the observation of a polar low that has a pair of ascending-descending flows like an extratropical cyclone. Mansfield (1974) and Duncan (1977) performed linear stability analyses to explain the small horizontal scale of polar lows. However, these analyses did not consider the effect of condensational heating. Although we will not discuss the initial triggering mechanism of the polar low in the present study, it should be noted that several mechanisms such as an upper-level short-wave trough (Montgomery and Farrell 1992; Grønås and Kvamstø 1995; Moore and Vachon 2002) and orography (Lee et al. 1998) are suggested.

Recently, numerical simulations have demonstrated that several physical processes operate simultaneously during polar low development. In particular, a sensitivity experiment, in which a certain physical process such as convective heating or sea surface heat fluxes is switched on/off, has contributed to understanding the polar low dynamics (Albright and Reed 1995; Pagowski and Moore 2001; Yanase et al. 2004). For example, Sardie and Warner (1985) showed that condensational heating and surface heat fluxes were necessary for the development of an Atlantic polar low, while the baroclinicity played an important role only at the initial stage. Since the relative importance of each process can complicatedly differ from case to case in the real atmosphere, it has been difficult to completely understand polar low dynamics.

An idealized experiment, in which the atmospheric field is simplified and only a few mechanisms are considered, is a promising approach to understand the interaction among important mechanisms. By using a slab-symmetric linear model in which the CISK-type parameterization for convective heating is incorporated, Sardie and Warner (1983) demonstrated that an interaction between CISK and baroclinic instability can explain the growth rate and horizontal scale of observed polar lows more realistically. However, the slab-symmetric linear analysis with CISK-type cumulus parameterization may not be realistic to represent condensational heating associated with organized cumulus convection, which is important to understand the detailed structure and dynamics of polar lows.

Recently, Yanase and Niino (2005; hereafter YN05) reported preliminary results of an idealized numerical experiment in which a polar low develops only through the baroclinic instability and diabatic effects within a simplified atmosphere. Though this configuration is similar to that of Sardie and Warner (1983), the approach here is fully nonlinear: a three-dimensional nonhydrostatic model with fine grid spacing of 2 or 5 km is used in order to represent the organized cumulus convection more realistically. It is found that, when the baroclinicity of the basic state is absent, a hurricane-like vortex with spiral cloud bands, a cloud-free eye, and a warm core develops. When the baroclinicity is strong, on the other hand, a vortex with a comma-shaped cloud and larger horizontal scale develops. The relation between cloud patterns and baroclinicity in the idealized numerical experiments showed good agreement with that in observations. YN05 briefly summarized the dependence of the cloud pattern, three-dimensional structure, and growth rate on baroclinicity.

The present study reports more detailed analysis of the idealized experiment, focusing on the relation between the environment field and vortex dynamics including 1) budget analyses on energy, vorticity, and heat; 2) influence of physical processes, such as diabatic heating and surface friction on the development and structure of the vortex; and 3) dependence of the vortex development on the initial disturbance and basic state, such as stratification and mean temperature. This paper is organized as follows: the numerical model and experimental design are described in section 2, the results are presented in section 3, detailed discussions are made in section 4, and a summary and conclusions are given in section 5.

2. Numerical model and experimental design

a. Model description

The three-dimensional nonhydrostatic model used for the present numerical experiment is the Meteorological Research Institute/Numerical Prediction Division Nonhydrostatic Model (MRI/NPD-NHM; Saito et al. 2001). A version with an anelastic equation system is used because it is sophisticated enough to describe the dynamics with density variation in the vertical direction, and yet sufficiently simple to analyze the energy budget compared to a version with a fully compressible system. The cloud physics scheme considers the mixing ratios of water vapor, cloud water, cloud ice, rain, and snow (Lin et al. 1983; Murakami 1990). The sensible and latent heat fluxes from the sea surface are calculated by the bulk formula of Kondo (1975). The subgrid

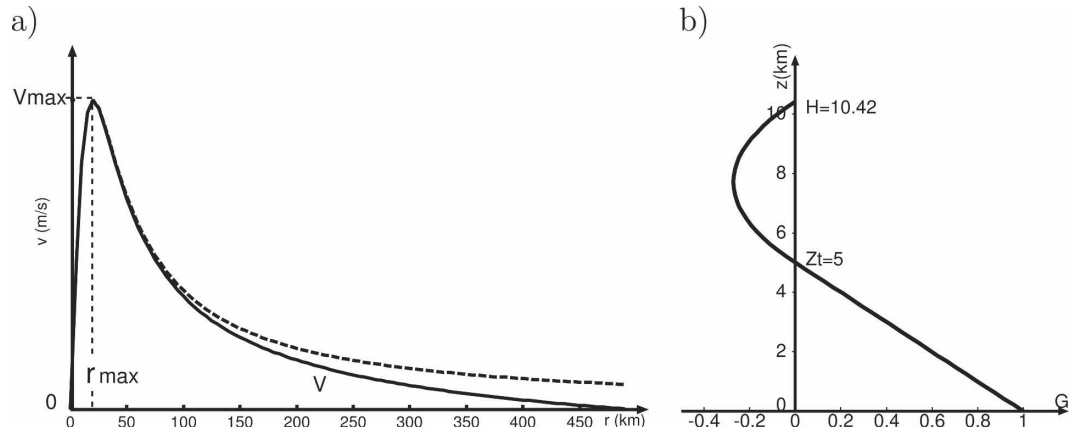


FIG. 1. (a) Radial distribution of the tangential velocity of the initial vortex near the sea surface level (solid line) where the distribution given by Eq. (2) (dashed line) is modified to vanish at the horizontal boundary of the calculation domain ($r = 500$ km). The latter is used for the experiment. (b) Vertical distribution of function $G(z)$ as given by Eq. (3).

turbulence is calculated by the closure formula of Deardorff (1980).

The size of the calculation domain used for the experiments is $1000 \text{ km} \times 1000 \text{ km}$ in the horizontal directions and 10.42 km in the vertical direction. The zonal boundary condition is cyclic. The meridional and vertical boundary conditions are rigid, and there are no fluxes of momentum, sensible heat, and latent heat at these boundaries except at the lower boundary. Near the top of the model domain, Rayleigh damping is applied to suppress the reflection of gravity waves. In the present experiment, the stratification above 5 km above sea level (ASL) is so strong that the existence of the top boundary at 10.42 km ASL has little effect on the polar low dynamics. Several additional experiments with the horizontal domain of $2000 \text{ km} \times 2000 \text{ km}$ revealed that the vortex characteristics such as growth rate, movement, and cloud pattern are little affected by the zonal and meridional sizes of the calculation domain, as far as they are larger than 1000 km .

The horizontal grid interval in the present study is 5 km in order to save the computation time for performing a large number of sensitivity experiments. YN05 demonstrated that a simulation with horizontal grid interval of 2 km better reproduces individual convective cells in spiral bands than one with a grid interval of 5 km . However, the difference in the meso- α -scale ($200\text{--}2000 \text{ km}$; Orlanski 1975) and meso- β -scale ($20\text{--}200 \text{ km}$) dynamics between the two simulations is found to be less significant. There are 26 layers in the vertical direction and the vertical grid interval increases linearly from 40 m at the lowest level to 760 m at the highest level of the calculation domain (i.e., 40, 70, and 100 m, etc.).

The time integration is started by imposing an axisymmetric vortex, which is in gradient-wind balance with the potential temperature field, at the center of the calculation domain. The structure of the vortex is the same as that used by Emanuel and Rotunno (1989) except for the sizes and amplitude: the tangential wind is given by

$$V = V_{\max} F(r) G(z), \quad (1)$$

where V_{\max} is 7 m s^{-1} ,

$$F(r) = \frac{2r/r_{\max}}{1 + (r/r_{\max})^2}, \quad (2)$$

$$G(z) = \begin{cases} \left(1 - \frac{z}{z_t}\right) & \text{for } z \leq z_t \\ \frac{H}{z_t} \left(1 - \frac{z}{H}\right) \left(\frac{z_t - z}{H - z_t}\right) & \text{for } z > z_t, \end{cases} \quad (3)$$

$r_{\max} = 20 \text{ km}$, $z_t = 5 \text{ km}$, and $H = 10.42 \text{ km}$ (Fig. 1). The tangential wind given by Eqs. (1) and (3) is largest near the sea surface (Fig. 1b). To make the tangential velocity vanish at the outer boundary r_{out} ($=500 \text{ km}$) the radial distribution of the tangential velocity in Eq. (2) is multiplied by $\cos(\pi r/2r_{\text{out}})$ (also see Fig. 1a). In some experiments, the strength V_{\max} or the radius r_{\max} is changed (see section 3).

b. Design of the basic state

We consider a zonally uniform basic state having a homogeneous meridional gradient of potential temperature that satisfies the thermal wind balance with the zonal wind of constant vertical shear. The Coriolis

parameter is assumed to be constant (*f* plane) with the value at 70°N, $1.36 \times 10^{-4} \text{ s}^{-1}$. Figure 2 shows the vertical profiles of potential temperature, relative humidity, and zonal wind in the basic state at the meridional center of the calculation domain. The potential temperature of the atmosphere near the sea surface is 270 K, a typical value at high latitude during a cold air outbreak in winter time. The vertical gradient of the potential temperature is horizontally uniform and is 1 K km^{-1} below 5 km ASL and 10 K km^{-1} above 5 km ASL. This choice is based on several previous observations that the stratification of the environment atmosphere is weak below 5–7 km ASL and is strong above this level (e.g., Emanuel and Rotunno 1989; Businger and Baik 1991).

The most important variable parameter in the present study is the vertical shear of the zonal wind, which represents the baroclinicity of the basic state. Typically observed values of vertical shear of the zonal wind in the polar low environment range from 0 to $4 \times 10^{-3} \text{ s}^{-1}$ (cf. Sardie and Warner 1983; Craig and Cho 1988) with an average value of $\sim 2 \times 10^{-3} \text{ s}^{-1}$ (Forbes and Lottes 1985). The sea surface temperature is set to be 10 K larger than the basic potential temperature of the atmosphere near the sea surface, thus having the same meridional gradient as that of the basic potential temperature of the atmosphere.

The relative humidity of the basic state (Fig. 2) decreases linearly from 50% near the sea surface to 0% at 5 km ASL, and remains 0% above 5 km ASL. Although this vertical profile of the relative humidity is somewhat different from that for the real mixed layer, it approaches the realistic one within a few hours after the time integration is started.

As the time integration is continued, the stratification and baroclinicity of the basic state are deformed. Such a deformation of the basic state may also occur in the real atmosphere. Since this makes the interpretation of the results difficult, however, we introduced a linear damping that operates only on the deviation of the zonal mean of the velocity and potential temperature fields from the basic state. The *e*-folding time of the linear damping is taken to be 5 h. We have also performed experiments without linear damping and have confirmed that the introduction of damping does not significantly alter the vortex dynamics discussed in the present study.

c. The control experiments

The experiments that have the basic state and the initial vortex as described in the previous subsections will hereafter be called the control experiments. The control experiments have only two parameters that

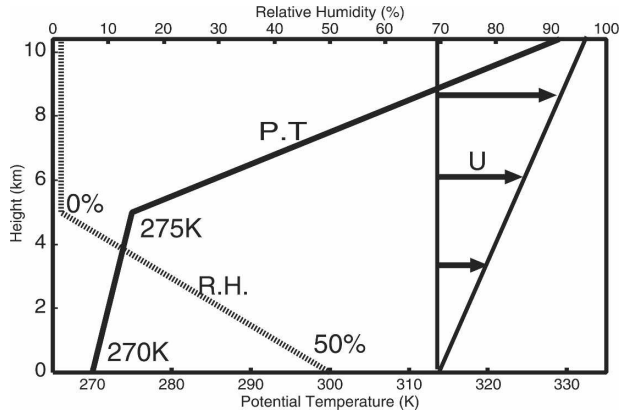


FIG. 2. Vertical profiles of potential temperature, relative humidity, and zonal wind in the basic state at the meridional center of the calculation domain. The solid line shows the potential temperature (the unit is K; the scale is shown at the bottom of the figure), the dotted line shows the relative humidity (the unit is percent; the scale is shown at the top of the figure). Line with arrows show the zonal wind that vanishes at the sea surface level and a uniform vertical shear.

characterize the presence/absence of the moist process and the magnitude of baroclinicity, and thus are denoted by a combination of two characters. The first character is either M or D, which denotes moist or dry, respectively. In the moist experiments, full physical processes are considered. In the dry experiments, on the other hand, both condensational heating and sea surface heat fluxes are switched off in order to examine the pure adiabatic dynamics of the vortex. The second character is a numeral and gives the magnitude of the baroclinicity (the vertical shear of the zonal flow) in the unit 10^{-3} s^{-1} . For example, experiment M3 denotes a moist experiment in which the vertical shear of the zonal flow is $3 \times 10^{-3} \text{ s}^{-1}$. Considering typically observed values of the environmental baroclinicity for polar lows, we perform seven experiments having different baroclinicity: experiments M0, M0.5, M1, M1.5, M2, M3, and M4. Although the dry experiments and no-baroclinicity experiment (M0) may be less realistic, they provide a good basis for understanding the vortex dynamics.

d. Energy budget analysis

The idealized experiment using a zonally cyclic boundary condition makes it possible to analyze reliable budgets of eddy kinetic energy (EKE) and eddy available potential energy (EPE). In the present study, the EKE is defined as

$$K_e \equiv \rho_0 \frac{\overline{u'^2} + \overline{v'^2} + \overline{w'^2}}{2}, \quad (4)$$

where u , v , and w are the zonal, meridional, and vertical components of the velocity, respectively, and ρ_0 the reference density, which is a function of z only. The overbar denotes the zonal average, and the prime the deviation from the zonal average. The EPE is defined as

$$P_e \equiv \frac{\alpha \overline{\theta'}^2}{2}, \quad (5)$$

where θ is the potential temperature and

$$\alpha \equiv \frac{g}{\theta_0} \frac{\partial(\theta_0 + \bar{\theta})}{\partial z}$$

(θ_0 is the reference potential temperature, also a function of z only).

The equation for the EKE budget becomes

$$\frac{\partial K_e}{\partial t} = [P_e, K_e] + [K_m, K_e] + \text{diss.} \quad (6)$$

The term $[P_e, K_e]$

$$\left(\equiv \frac{\rho_0 g}{\theta_0} \overline{w' \theta'} \right)$$

in the right-hand side (rhs) is the conversion from EPE to EKE. The term $[K_m, K_e]$

$$\left(\equiv -\rho_0 \frac{\partial \bar{u}}{\partial z} \overline{u' w'} \right)$$

is the conversion from mean kinetic energy (MKE) to EKE. Note that $[K_m, K_e]$ is due to an ageostrophic effect and is absent in a quasigeostrophic system (cf. Yanase and Niino 2004). The term “diss” is the subgrid-scale dissipation. The time derivative of K_e at time t has been calculated by

$$\frac{\partial K_e}{\partial t} \equiv \frac{K_e(t + \Delta t) - K_e(t)}{\Delta t},$$

where $\Delta t = 5$ h, which is the time interval of data output. The equation for the EPE budget is similarly written as

$$\frac{\partial P_e}{\partial t} = [P_m, P_e] + [Q, P_e] + [K_e, P_e] + \text{diss.} \quad (7)$$

The term $[P_m, P_e]$

$$\left(\equiv -\alpha \frac{\partial \bar{\theta}}{\partial y} \overline{v' \theta'} \right)$$

is the conversion from mean available potential energy (MPE) to EPE, $[Q, P_e]$

$$\left(\equiv \frac{\alpha \theta_0}{c_p T_0} \overline{q' \theta'}; q \text{ is the condensational heating} \right)$$

the generation of EPE by condensational heating, and the term $[K_e, P_e]$

$$\left(\equiv -\frac{\rho_0 g}{\theta_0} \overline{w' \theta'} \right)$$

is the conversion from EKE to EPE, which is equal to $-[P_e, K_e]$ in Eq. (6).

3. Results

In this section, we will show the results of experiments M0, M0.5, M1, M1.5, M2, M3, and M4. First, we overview the effect of baroclinicity on vortex characteristics such as growth rates, cloud patterns, and energy budgets in section 3a. Next, we describe the detailed structure and dynamics of the vortex for experiments M0, M1, and M3, which represent the cases with zero, intermediate, and strong baroclinicity, respectively, in sections 3b–d.

In the following, our analysis will be confined to the characteristics of the entire vortex (meso- α scale) and its inner structures (meso- β scale) such as cloud bands, fronts, and a cloud-free eye. Although the present simulation with horizontal grid spacing 5 km crudely resolves meso- γ -scale motions such as convective cells, these motions result in very noisy fields. We therefore average the data over the horizontal scale of 20 km for showing structures, while averaging over the horizontal scale of 50 km and vertically 1 km for analyzing the energy budget.

a. Overview of the control experiments

1) BASIC CHARACTERISTICS

Figure 3a shows the time evolution of the EKE for several control experiments (M0–M4). The initial vortex for all of the experiments develops with time. In particular, the vortex develops even in the absence of the baroclinicity (M0). As the baroclinicity is increased, the growth rate of the vortex increases. There is no drastic regime shift that causes any discontinuous change in the growth rate between M0 and M4.

Figure 4 shows “cloud patterns” defined by the vertical integration of total condensed water (i.e., the sum of cloud water, cloud ice, rain, and snow) for all the control experiments at their development stages. In the absence of the baroclinicity (experiment M0: Figs. 4a and 4h), the vortex has a nearly axisymmetric cloud pattern with the horizontal scale of ~ 300 km. As the baroclinicity is increased (from Figs. 4a to 4g), the cloud pattern asymmetry increases and the horizontal scale increases. For experiments M2–M4, the vortex has a

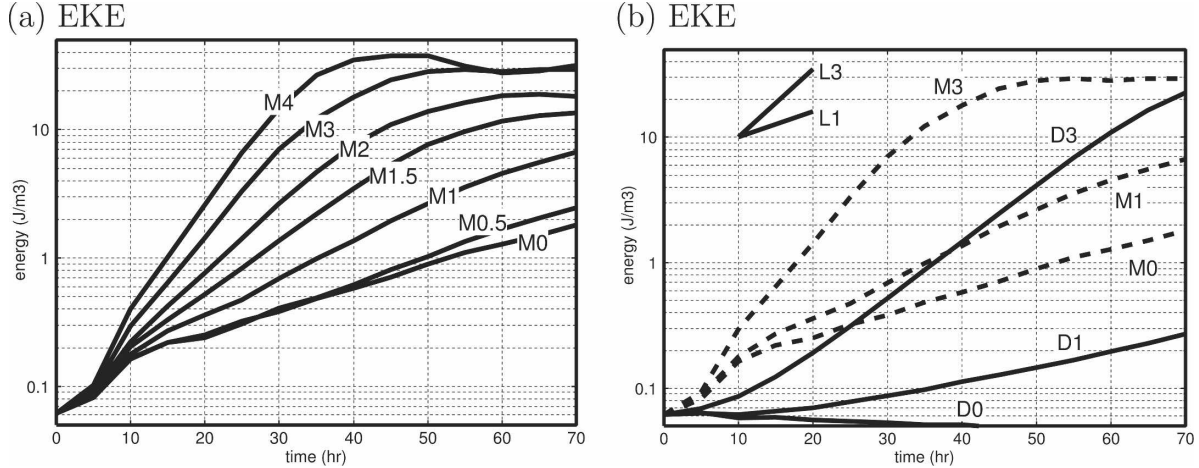


FIG. 3. Time evolution of the EKE (J m^{-3}) averaged over the whole calculation domain of $1000 \text{ km} \times 1000 \text{ km} \times 10.42 \text{ km}$: (a) the control experiments (M0–M4; YN05). (b) Dry experiments D0, D1, and D3 (solid lines) and corresponding moist experiments M0, M1, and M3 (dashed lines). The straight lines in the upper-left corner give the growth rates predicted by the linear theory: In expts L1 and L3, the same magnitudes of the basic baroclinicity as that in expts D1 and D3, respectively, are assumed in the nongeostrophic nonhydrostatic linear model (Tokioka 1973; Yanase and Niino 2004), where the zonal wavelength, meridional half wavelength, and vertical scale of the disturbance are assumed to be 1000, 1000, and 5 km, respectively.

comma-shaped cloud pattern in which a cloud band develops on the northern and eastern sides of the low center. As a whole, a variety of cloud patterns observed in nature are well reproduced in the typical range of the baroclinicity of the basic state.

Figure 5 shows the vortex movements for the control experiments. In experiment M0 for which no baroclinic flow exists, the vortex simply stays at the same place where the vortex is initially located. When the baroclinicity is large, the vortex moves eastward due to the advection by the strong westerly flow in the basic state (see Fig. 2). In experiments M0.5–M2 in which the baroclinicity is intermediate, however, the vortex exhibits a tendency to move northward in addition to the eastward motion. This tendency will be investigated in section 3d.

The difference of the growth rate among M0–M4 in Fig. 3a is expected to result from the difference of the EPE and EKE budgets. Figures 6a–c compare the time evolution of the EPE budget among the control experiments. Among the terms in the right hand side of Eq. (7), the condensational heating $[Q, P_e]$ has nearly similar “normalized” magnitude fluctuating between 60 and $100 \times 10^{-6} \text{ s}^{-1}$ for all experiments. The relative importance of $[P_m, P_e]$, on the other hand, becomes large as the baroclinicity is increased. A part of EPE is converted to the EKE through the term $[K_e, P_e]$ and some is lost by the subgrid-scale dissipation (diss). Figures 6d–f show the time evolution of the EKE budget. The generation of EKE from EPE, $[P_e, K_e]$, is dominant for all the experiments. The term $[K_m, K_e]$, on the other

hand, becomes large as the baroclinicity is increased. This term represents the conversion of the kinetic energy of the vertical shear of the basic zonal flow. Again, some of the EKE is lost by the subgrid dissipation (diss). Both $[P_m, P_e]$ in the EPE budget and $[K_m, K_e]$ in the EKE budget become monotonically large, as the baroclinicity is increased from M0 to M4 (not shown).

2) EFFECTS OF CONDENSATIONAL HEATING AND SEA SURFACE FLUXES

To examine the effect of condensational heating and sea surface heat fluxes, dry experiments, D0, D1, and D3 are performed. Figure 3b shows the time evolution of EKE for these experiments. For all experiments, the growth rates turn out to be smaller than those for the corresponding moist experiments, demonstrating that diabatic heating promotes vortex development. The vortex in experiment D0 declines since there is no baroclinic energy source. The vortex in experiment D1 and D3 develops through the baroclinic energy conversion. The lines L1 and L3 in Fig. 3b indicate the growth rates of dry baroclinic waves predicted by the linear theory. The growth rate for experiment D3 is nearly the same as that for L3. This shows that the vortex in experiment D3 develops through baroclinic instability, and diabatic heating enforces the development of baroclinic waves in experiment M3. The detailed difference of structures and dynamics between experiments D3 and M3 are further examined in section 3c. The growth rate for experiment D1 is slightly weaker than that for the esti-

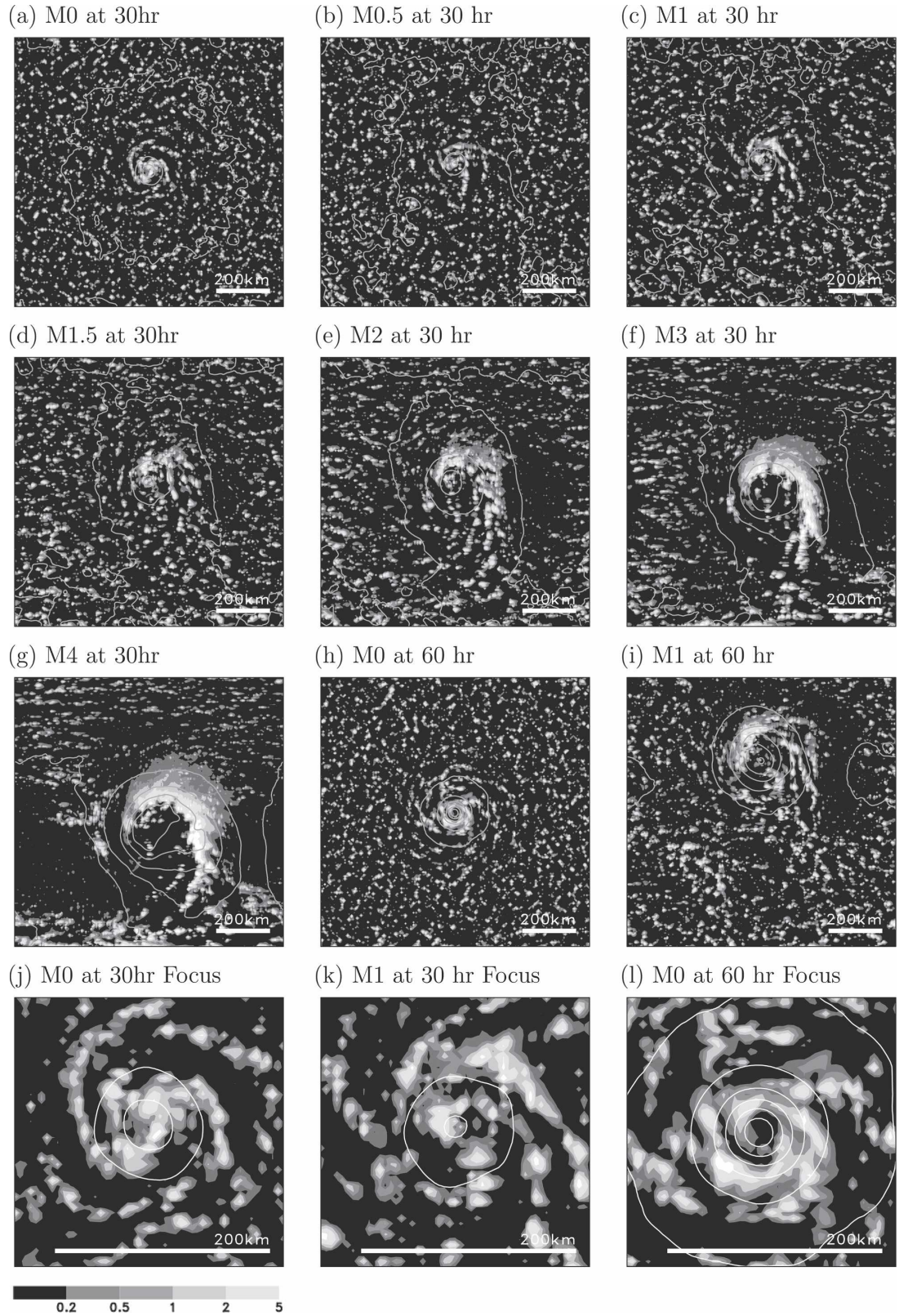


FIG. 4. Vertically integrated total condensed water (shade; the unit is kg m^{-2}) and SLP (contour interval 3 hPa) for the control experiments. (a)–(i) The whole calculation domain is shown, while the focused views (a), (c), and (h) near the low center are shown in (j), (k), and (l), respectively. The low pressure center is located at the zonal center of the figure by utilizing the cyclic boundary condition. (f), (h), (i) Taken from YN05.

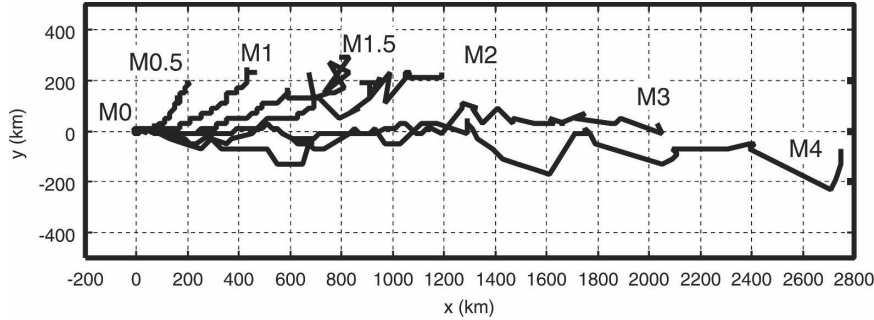


FIG. 5. Movements of the low center for the control experiments. Note that the low travels more than 1000 km in the zonal direction across the cyclic boundary. The origin indicates the initial vortex center.

mation L1 because of the dissipation present in the numerical model.

3) EFFECTS OF SURFACE FRICTION

Surface friction is known to play an important role in the vortex dynamics of a tropical cyclone by causing convergence in the Ekman layer. To examine the effect

of the surface friction on polar lows, we have performed sensitivity experiments in which the surface friction is eliminated (i.e., a free-slip condition is assumed at the lower boundary). Figure 7a shows the time evolution of EKE for these experiments, which are referred to as M0-NOFRIC, M1-NOFRIC, and M3-NOFRIC, each corresponding to the control experiments M0, M1, and M3, respectively. The EKE in each experiment without

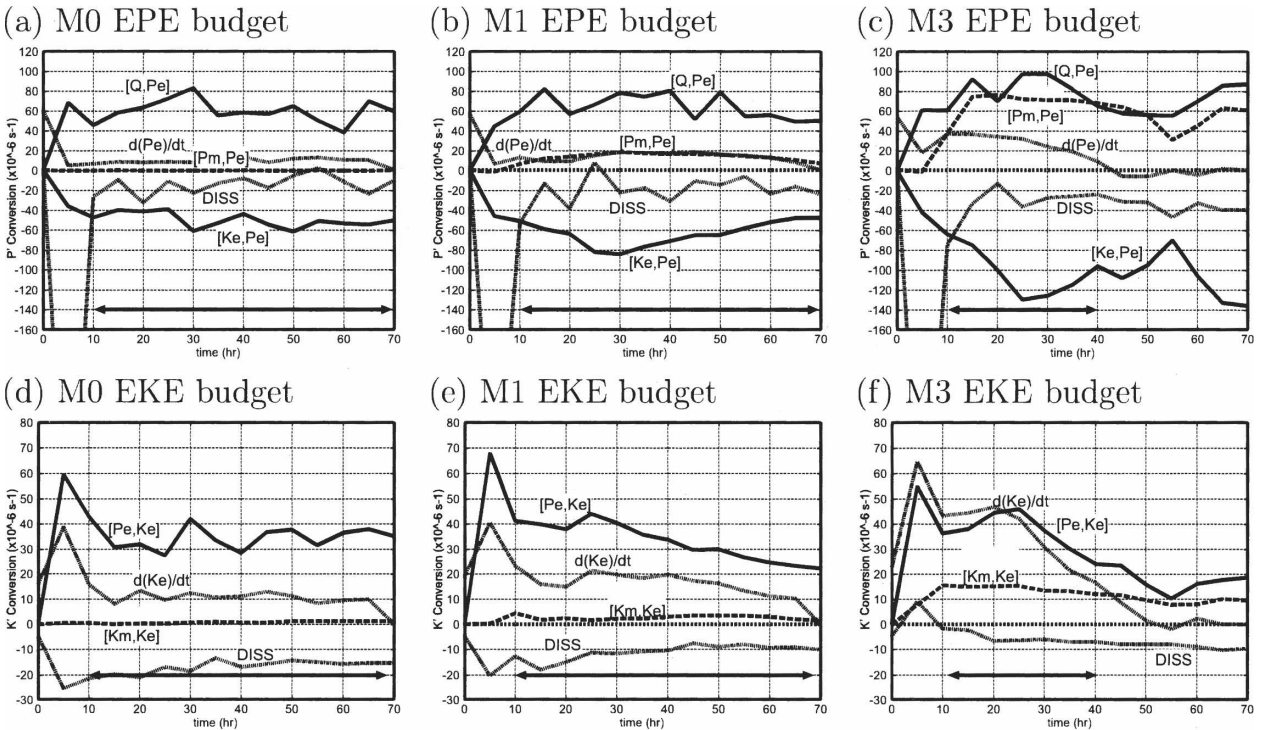


FIG. 6. Time evolution of the terms in the equation of the EKE and EPE budgets for three control experiments; each term is divided by the instantaneous value of EPE or EKE and has a unit of 10^{-6} s^{-1} . The EPE budget for (a) M0, (b) M1, and (c) M3. The EKE budget for (d) M0, (e) M1, and (f) M3. The arrow near the bottom of each panel shows the development stage of the vortex. Note that $[K_e, P_e]$ in (a)–(c) does not have the same magnitude as $[P_e, K_e]$ in (d)–(f), respectively, because of the normalization: the former (the latter) is divided by an instantaneous value of EPE (EKE). During the initial 10 h, small-scale convection causes extremely large negative value of diss so that it is difficult to discuss the detailed energy budget of the vortex during this period.

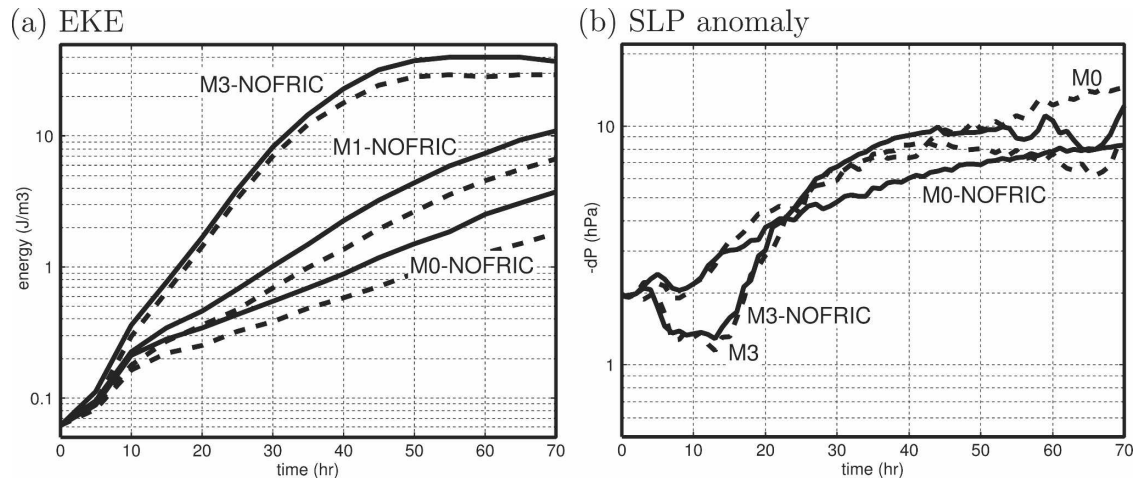


FIG. 7. Time evolution of the (a) EKE and (b) negative SLP anomaly for expts M0-NOFRIC, M1-NOFRIC, and M3-NOFRIC (solid lines), and for expts M0, M1, and M3 (dashed line). Note that in the lines for expts M1 and M1-NOFRIC are not shown in (b) for the sake of clarity.

surface friction is found to increase more rapidly than that in the corresponding experiment with surface friction. This shows that the energy loss by surface friction simply reduces the growth rate.

Figure 7b, on the other hand, shows the time evolution of the sea level pressure (SLP) anomaly at the low center for experiments M0, M3, M0-NOFRIC, and M3-NOFRIC. It is consistent with the growth rate based on EKE (Fig. 7a) that the SLP anomaly for experiment M3-NOFRIC develops faster than that for experiment M3 except for the first 15 h of the period: the EKE decreases initially, because the initial vortex is not the fastest growing mode. In M0-NOFRIC, however, the SLP anomaly develops slower than that for M0, showing that the surface friction promotes the vortex development for experiment M0. The detailed difference of structures and dynamics between M0 and M0-NOFRIC are described in section 3b. The results for M1 and M1-NOFRIC (only shown for EKE) are intermediate between those for M0 and M3.

b. No baroclinicity case (experiment M0)

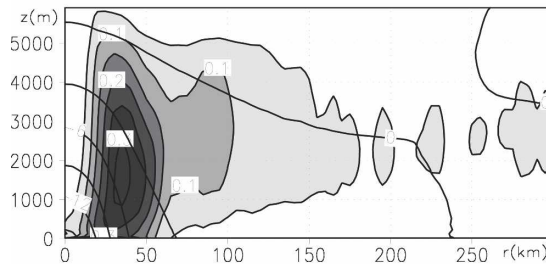
For experiment M0, in which the baroclinicity of the basic state is absent, we have shown in Figs. 4a and 4h that a vortex with a nearly axisymmetric cloud pattern does develop in a three-dimensional simulation and that the surface friction promotes the vortex development. Emanuel and Rotunno (1989) used an axisymmetric nonhydrostatic model with a horizontal resolution of 10 km to show that a hurricane-like vortex can develop in a typical polar low environment and that the vortex development is sensitive to the initial perturbation. In this subsection, we will look at the detailed

structure of the vortex, the effect of surface friction, and sensitivity to the initial perturbation.

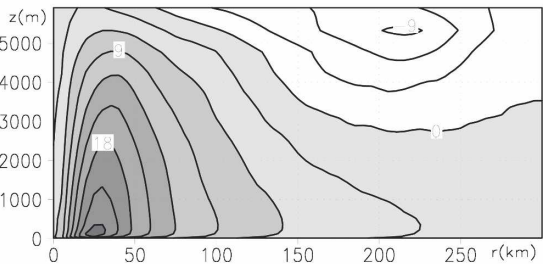
1) VORTEX STRUCTURE

Figure 8 shows the radial–vertical cross sections of the azimuthal-mean variables averaged between 60 and 70 h for experiment M0. The amount of the total condensed water is largest at radius $r = 20\text{--}50$ km (Fig. 8a), which corresponds to the eyewall region in Fig. 4l. On the other hand, the amount of condensed water is small in the cloud-free eye region near the low center ($r < 10$ km). The maximum tangential velocity is 25 m s^{-1} at 150 m ASL, $r = 25$ km (Fig. 8b). The radial and vertical flows (Figs. 8c and 8d) show the structure of the secondary circulation: the air strongly converges toward the low center near the sea surface with maximum amplitude of 9 m s^{-1} , then ascends at $r = 20\text{--}50$ km, and flows outward above 4 km ASL. A weak downdraft is seen for $r < 10$ km, where the condensed water is small (Fig. 8a). The relative humidity for $r < 10$ km is also less than 50% above 2 km ASL (Fig. 8e) because of downward transport of dry air from the upper atmosphere (Fig. 8d). A remarkable positive anomaly of the potential temperature near the low center (a warm core structure; Fig. 8f) also results from the subsidence of high potential temperature air from the upper atmosphere. The warm core structure and the tangential wind increasing toward the sea surface (Fig. 8b) are consistent with the thermal wind balance (in a gradient wind sense). Note that the centrifugal force is one order of magnitude larger than the Coriolis force at the radius of the maximum tangential wind ($r = 25$ km). The

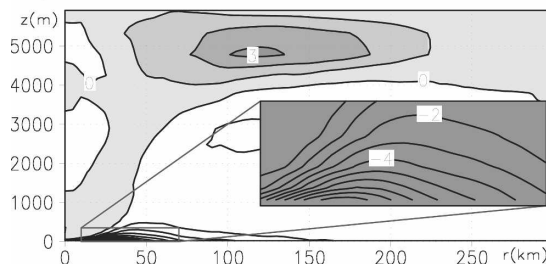
a) Condensed water and pressure



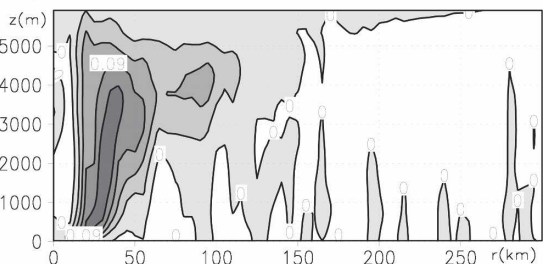
b) Tangential velocity



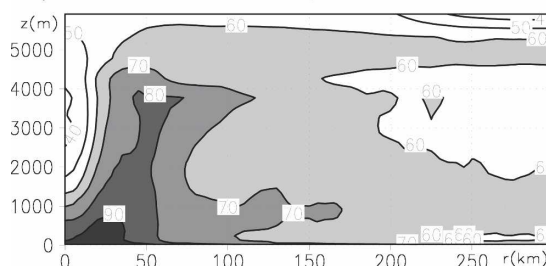
c) Radial velocity



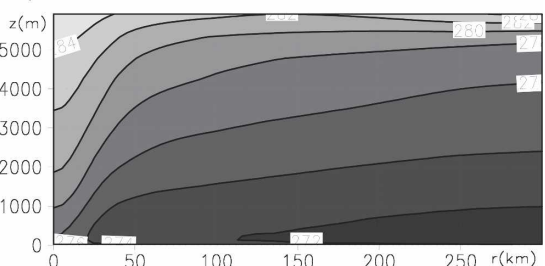
d) Vertical velocity



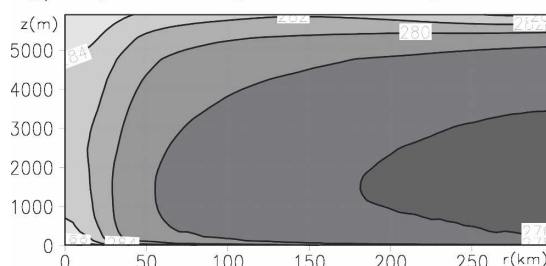
e) Relative humidity



f) Potential temperature



g) Equivalent potential temperature



h) Absolute angular momentum

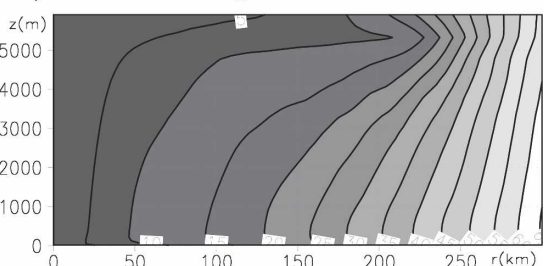


FIG. 8. Azimuthal-mean variables in the radial–vertical cross section averaged between 60 and 70 h for expt M0: (a) total condensed water (shade; contour interval is 0.05 g kg^{-1}) and pressure anomaly (solid line; contour interval is 3 hPa); (b) tangential velocity (contour interval is 3 m s^{-1}); (c) radial velocity (contour interval is 1 m s^{-1}); (d) vertical velocity (contour interval is 0.03 m s^{-1}); (e) relative humidity (contour interval is 10%); (f) potential temperature (contour interval is 2 K); (g) equivalent potential temperature (contour interval is 2 K); and (h) absolute angular momentum $M = rv + (f/2)^2$ (contour interval is $5 \times 10^{-5} \text{ m}^2 \text{ s}^{-1}$). In (c), the gray rectangle shows the detailed structure in the region with the radius between 10 and 70 km and the height between 0 and 350 m ASL.

equivalent potential temperature also shows a positive anomaly near the low center (Fig. 8g). Isopleths of the equivalent potential temperature are nearly vertical between $r = 20$ and 50 km . The isopleths of absolute angular momentum have a larger slope than that of the

equivalent potential temperature between $r = 20$ and 50 km (Fig. 8h), indicating that the atmosphere is unstable for moist slantwise convection. This is consistent with the intense updraft between $r = 20$ and 50 km (Fig. 8d) that tilts outward with height.

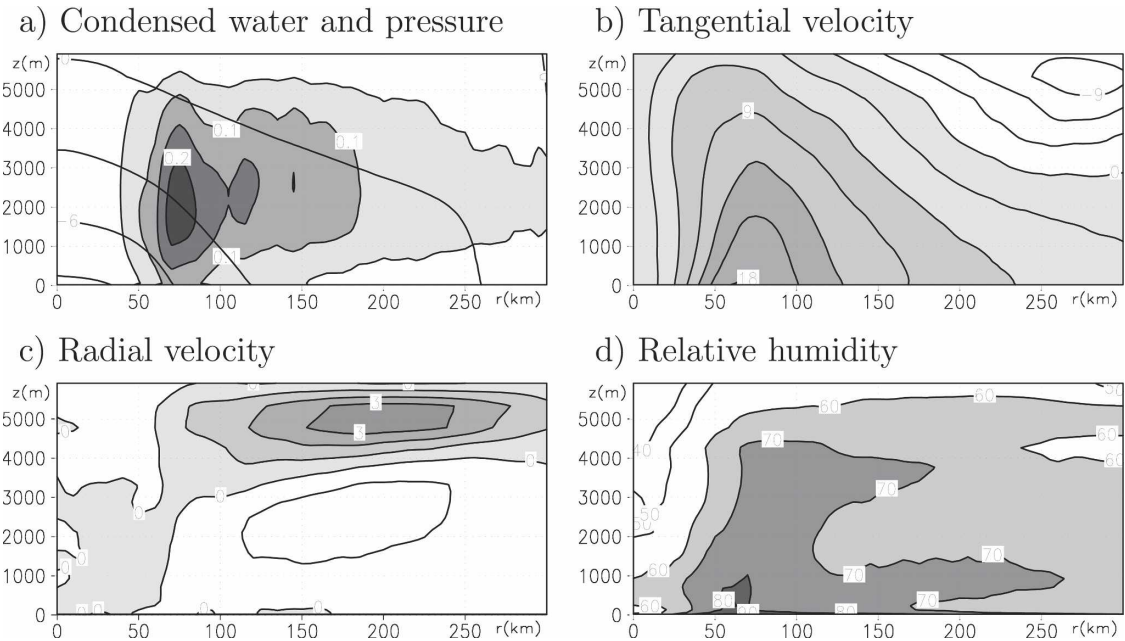


FIG. 9. Azimuthal-mean variables in the radial–vertical cross section averaged between 60 and 70 h for expt M0-NOFRIC: (a) total condensed water (shade; contour interval is 0.05 g kg^{-1}) and pressure anomaly (line; contour interval is 3 hPa); (b) tangential velocity (contour interval is 3 m s^{-1}); (c) radial velocity (contour interval is 1 m s^{-1}); and (d) relative humidity (contour interval is 10%).

2) EFFECT OF SURFACE FRICTION

We have seen in Figs. 7a and 7b that the time evolutions of EKE and SLP in experiment M0-NOFRIC show different tendencies. Figure 9 shows the azimuthal-mean variables in the radial–vertical cross section averaged between 60 and 70 h for experiment M0-NOFRIC. The pressure pattern for M0-NOFRIC (Fig. 9a) has a larger horizontal scale than that for experiment M0 (Fig. 8a), but its magnitude is smaller than that for M0. The maximum tangential wind for experiment M0-NOFRIC also occurs at larger radius than that for experiment M0. (Figs. 8b and 9b). In M0-NOFRIC, the removal of surface friction results in very weak inflow near the sea surface (Fig. 9c) in contrast to the strong inflow in the rotational boundary layer in M0 (Fig. 8c). The absence of the strong inflow in the rotational boundary layer results in a reduced transport of water vapor toward the low center (Figs. 8e, 9d), causing an outward shift of the convective region (Fig. 9a). Thus, the secondary circulation in experiment M0-NOFRIC occurs far from the low center compared to experiment M0. The absence of a strong inflow also reduces the transport of angular momentum into the low center, locating the maximum tangential wind far from the low center in experiment M0-NOFRIC (Fig. 9b). These results of experiment M0-NOFRIC show the importance of the surface friction for organizing

cumulus convection near the low center in experiment M0.

3) DEPENDENCE ON THE INITIAL VORTEX

In contrast to the experiments with strong baroclinicity (experiments M2–M4), the vortex in experiment M0 keeps its small horizontal scale of the initial vortex during its development (see Fig. 4). This implies that the vortex development in experiment M0 may have a strong dependence on the initial vortex. We have performed three additional experiments in which the size or amplitude of the initial vortex are varied, accordingly. In the control experiment M0, the initial vortex has the maximum tangential wind of $V_{\max} = 7 \text{ m s}^{-1}$ at $r_{\max} = 20 \text{ km}$ (section 2a). In experiment M0-V2, V_{\max} is reduced to 2 m s^{-1} . In experiments M0-R50 and M0-R100, V_{\max} is the same as that in M0, but r_{\max} is increased to 50 and 100 km, respectively.

Figures 10a and 10b show the time evolution of the EKE and SLP, respectively, for these four experiments. For experiment M0-V2, the initial vortex does not develop. The result that a weak vortex fails to develop is consistent with the previous results for an axisymmetric model (e.g., Emanuel and Rotunno 1989). For experiment M0-R50, the growth rate of the EKE is nearly the same as in M0, though the magnitude of EKE is much larger than that for M0 because of its larger initial size.

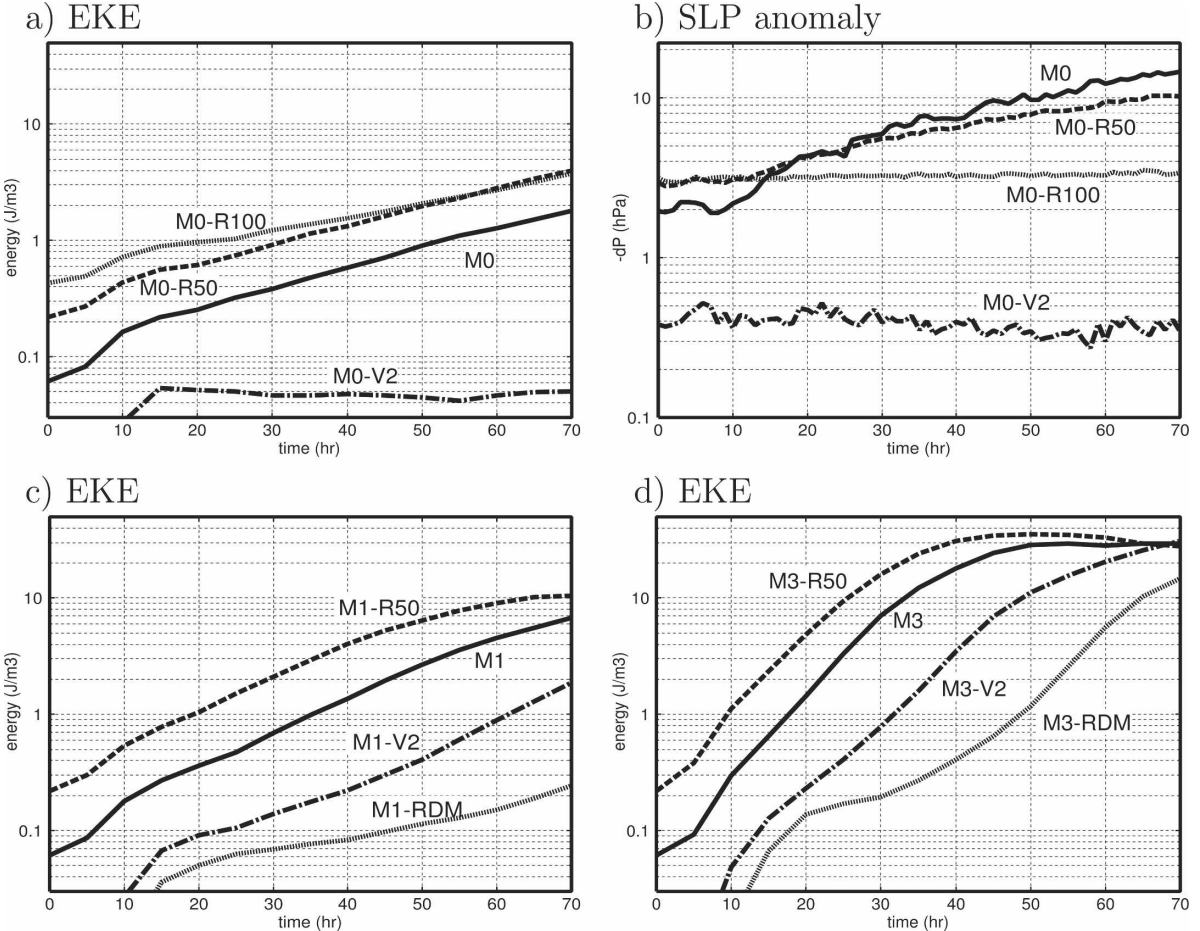


FIG. 10. Time evolution of (a) the EKE and (b) the SLP anomaly for the expts M0, M0-V2, M0-R50, and M0-R100; (c) EKE for the expts M1, M1-V2, M1-R50, and M1-RDM; and (d) EKE for the expts M3, M3-V2, M3-R50, and M3-RDM.

For experiment M0-R100, however, the growth rate of the EKE is considerably smaller than for experiments M0 and M0-R50. In the time evolution of SLP (Fig. 10b), it is more apparent that the growth rate decreases as the horizontal size of the initial vortex becomes large, which is consistent with the result by Emanuel and Rotunno (1989). Figures 11a–c show horizontal distributions of the cloud pattern at 60 h for experiments M0-V2, M0-R50, and M0-R100. The vortex in experiment M0-R50 has a larger horizontal scale than that in M0 (Fig. 4h), reflecting the difference in the horizontal scale of the initial vortex. The vortex in experiment M0-R100 appears to fail in its organization: a ring of deep convection propagates outward with time, which results in the absence of deepening of the SLP at the polar low center. The present result clearly shows that an initial vortex with small horizontal size is preferable for the development of a strong and well-organized vortex.

c. Strong baroclinicity case (experiment M3)

The cloud pattern in experiment M3 shows a comma shape that has a remarkable cloud band on the northern and eastern sides of the vortex (see Fig. 4f). This pattern resembles those of observed extratropical cyclones that develop by baroclinic instability at midlatitudes except that the horizontal scale is small for experiment M3. In this section, we will investigate the structure and dynamics of experiment M3 in detail by comparison with that of experiment D3, which develops purely through dry baroclinic instability. We will also examine the sensitivity of the vortex dynamics to initial perturbations.

1) STRUCTURE AND DYNAMICS

Figure 12 shows the vortex structures in the horizontal cross sections for experiments D3 and M3. Although the meridional scale of the SLP pattern for experiment

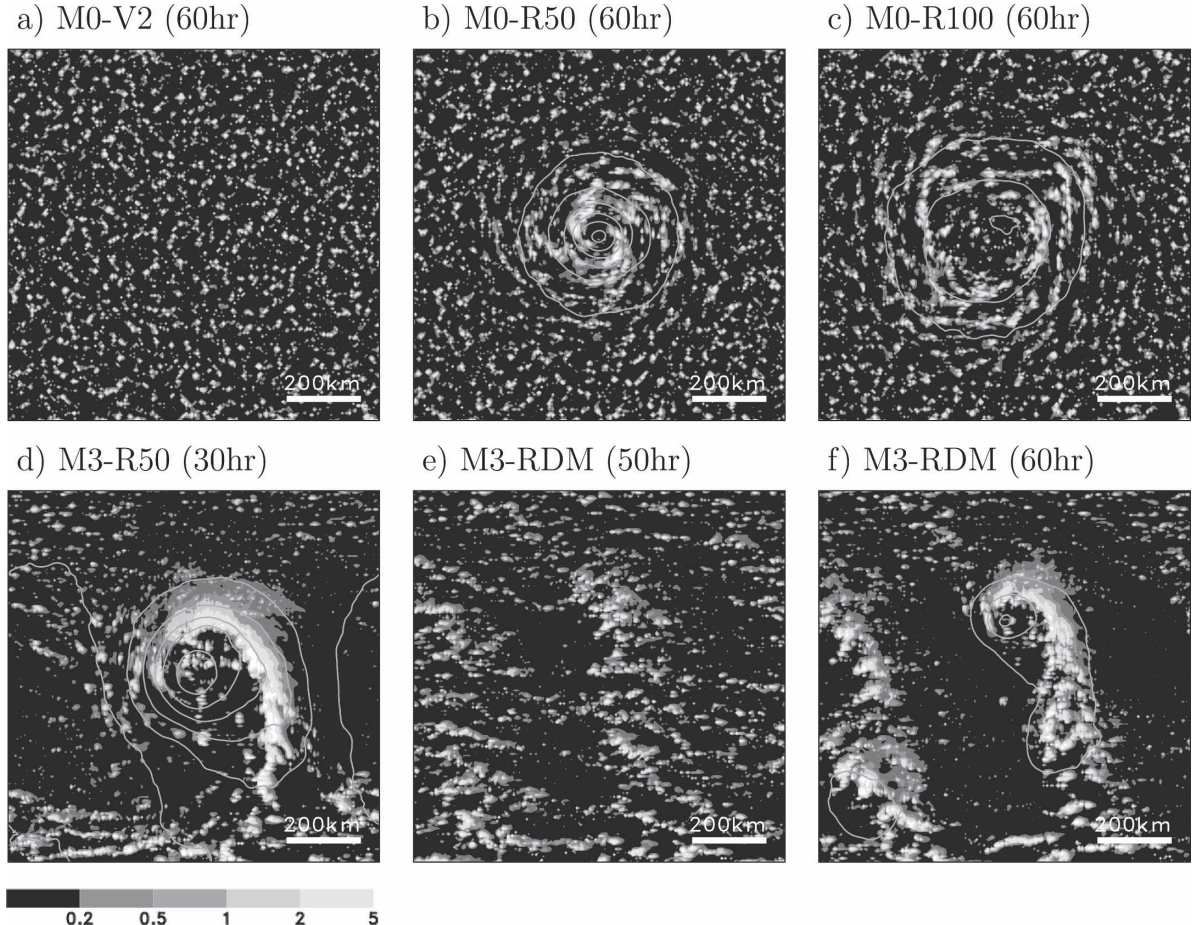


FIG. 11. Vertically integrated total condensed water (shade; the unit is g kg^{-1}) and SLP (contour interval is 3 hPa) for expts (a) M0-V2 (60 h); (b) M0-R50 (60 h); (c) M0-R100 (60 h); (d) M3-R50 (30 h); (e) M3-RDM (50 h); and (f) M3-RDM (60 h).

M3 (Fig. 12b) is larger than that for M0 (Figs. 4a and 4h), it is smaller than that for experiment D3; in D3, the low has a meridional scale as large as the whole meridional size of the calculation domain (Fig. 12a), which is consistent with dry baroclinic instability theory (Eady 1949) in that the wave with a larger meridional scale has a larger growth rate. For both experiments D3 and M3, the updraft occurs on the eastern side of the low center (Figs. 12c,d), which resembles a feature of the dry baroclinic instability wave in a quasigeostrophic system (Eady 1949) or in a nongeostrophic system with and without latent heating (Yanase and Niino 2004); in the baroclinic wave, the northward transport of warm air generates buoyancy on the eastern side of the vortex and results in the upward motion of the air. For experiment M3, however, the updraft occurs within a narrow band corresponding to the cloud band (Fig. 4f). For experiment D3, the upper-level trough exists to the west of the surface low center (Fig. 12e), which also

resembles a quasigeostrophic dry baroclinic wave. The upper-level trough for experiment M3 shows a similar feature on the meso- α scale (Fig. 12f). However, the pressure minimum in the upper-level trough is located right above the surface low center.

Figure 13 shows the zonal–vertical cross section through the low center for experiments D3 and M3. As was shown in Fig. 12, the trough axis for both D3 and M3 tilts westward with increasing height (Figs. 13a,b). With regard to the meso- β -scale structure, however, the trough axis in experiment M3 is nearly vertical near the low center. The updraft, as was shown in Fig. 12, occurs to the east of the trough for both D3 and M3 (Figs. 13c,d). In experiment M3, the updraft region occurs within the meso- β -scale band. In addition, a meso- β -scale downdraft occurs near the low center over a considerable depth between 0 and 5 km ASL in experiment M3, which is not seen in D3. In both D3 and M3 the warm air exists to the east of the low center and the

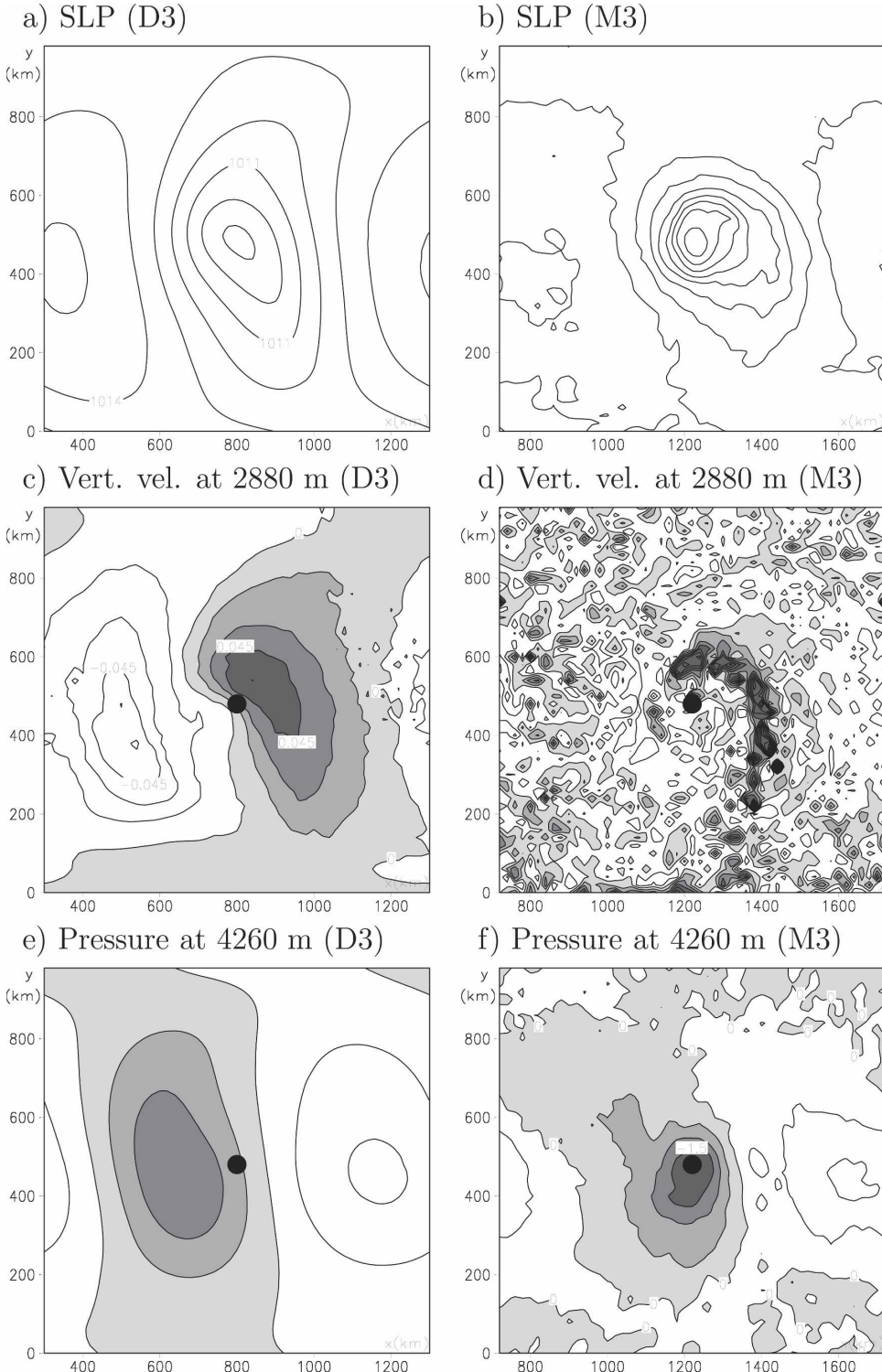


FIG. 12. Horizontal cross sections for (a), (c), (e) expt D3 at 50 h and (b), (d), (f) expt M3 at 30 h. (a), (b) The SLP (contour interval is 1 hPa); (c), (d) the vertical wind at 2880 m ASL for expt D3 (contour interval is 0.015 m s^{-1}) and expt M3 (contour interval is 0.1 m s^{-1}), respectively. The shaded regions indicate the positive value; (e), (f) the pressure anomaly at 4260 m ASL (contour interval is 0.5 hPa). The shaded regions indicate the negative value. The solid circle indicates the low center defined by SLP.

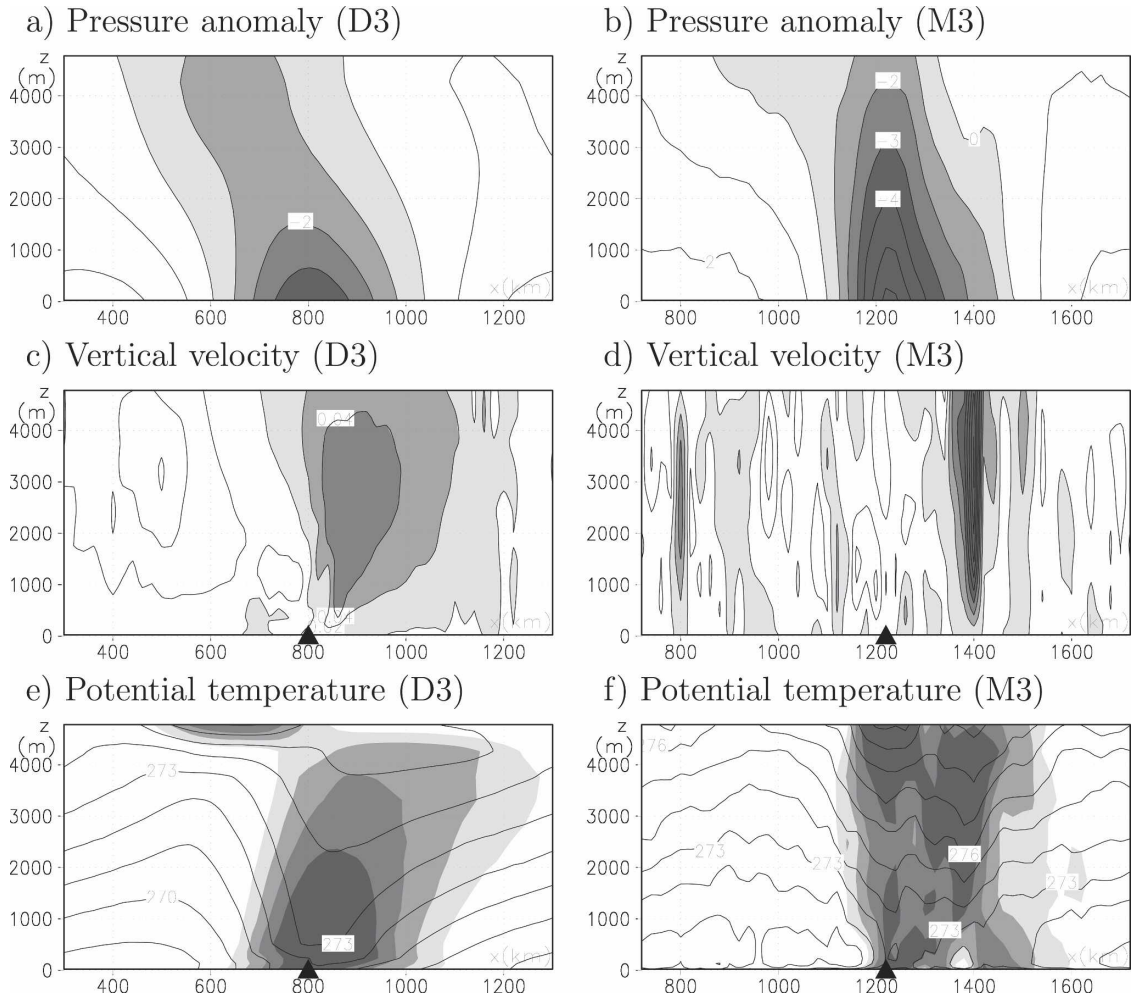


FIG. 13. Zonal-vertical cross sections through the low center for (a), (c), (e) expt D3 at 50 h and (b), (d), (f) expt M3 at 30 h. (a), (b) The pressure anomaly (contour interval is 1 hPa). The shaded regions indicate the negative value; (c), (d) vertical velocity (contour interval is 0.02 and 0.1 m s^{-1} , respectively). The shaded regions indicate the positive value; (e), (f) potential temperature (contour interval is 1 K). The shaded regions indicate the positive anomaly. The solid triangle indicates the low center defined by SLP.

cold air to the west (Figs. 13e,f). This meso- α -scale structure resembles that of a quasigeostrophic dry baroclinic wave. For experiment M3, however, a meso- β -scale warm core structure occurs near the low center between 0 and 5 km ASL.

To understand the structure of the vortex such as a deep warm core for experiment M3, we have investigated the balance of terms in the thermodynamic equations in the zonal–vertical cross section through the low center for experiments D3 and M3 (Fig. 14). First, let us look at experiment D3 (Figs. 14a,c,e). Here warm air advection and adiabatic cooling occur to the east of the low center, while there is cold air advection and adiabatic warming to the west (Figs. 14a,c). Since the meridional advection dominates the vertical advection for

experiment D3, the potential temperature anomaly is positive to the east of the low center, whereas it is negative to the west (see Fig. 13e). The zonal wind advection tilts the potential temperature field eastward with increasing height (Fig. 14e), as seen in Fig. 13e.

Now, let us look at experiment M3 (Figs. 14b,d,f,g). Warm air advection is strongest within the narrow convective region to the east of the low center (Fig. 14b; see also Fig. 13d), whereas cold air advection is strongest just to the west of the low center. The vertical advection shows a very complicated pattern but has generally larger magnitude than the meridional advection. Significant adiabatic cooling occurs within the narrow convective region to the east of the low center (Fig. 14d). This adiabatic cooling, however, is overwhelmed

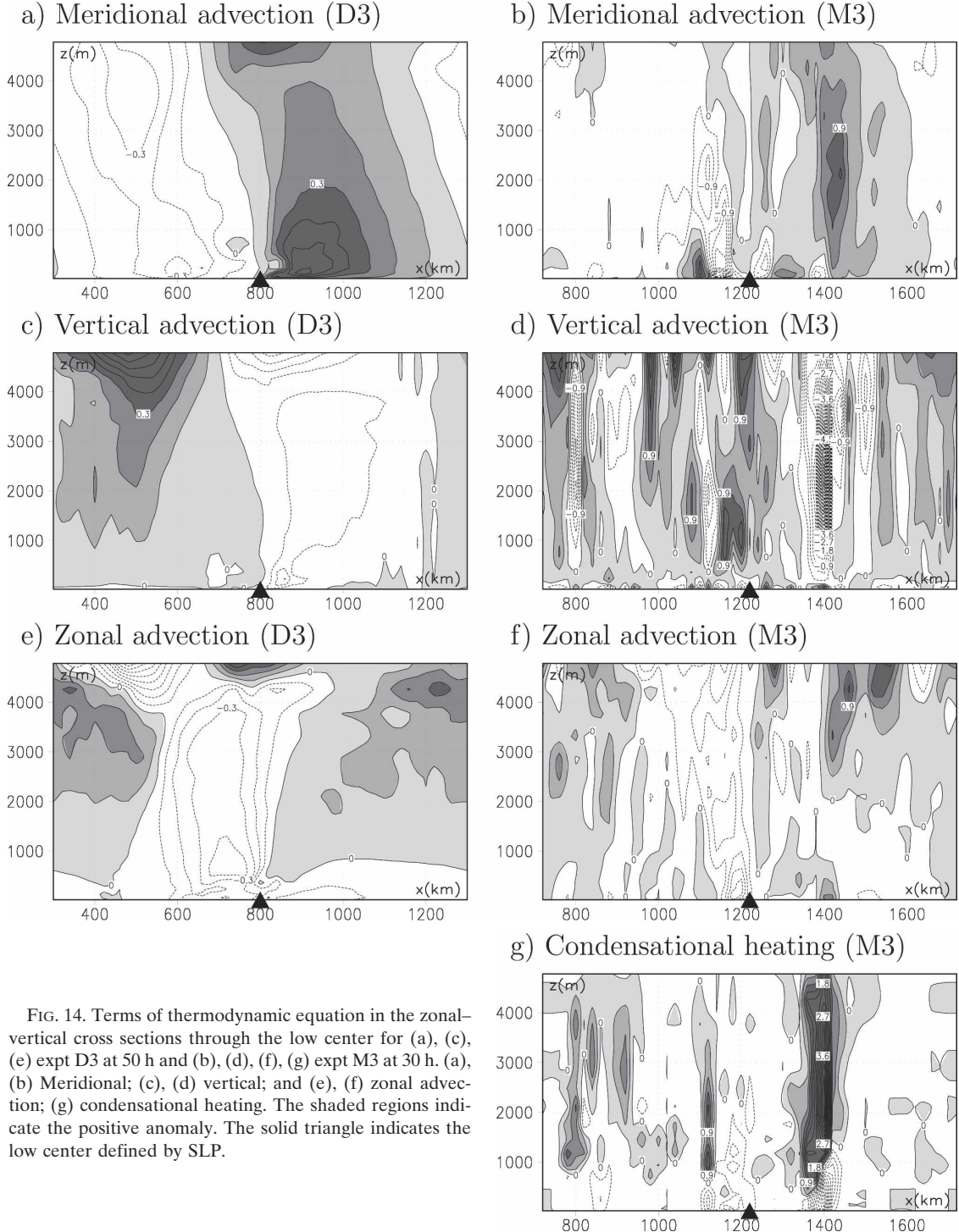


FIG. 14. Terms of thermodynamic equation in the zonal–vertical cross sections through the low center for (a), (c), (e) expt D3 at 50 h and (b), (d), (f), (g) expt M3 at 30 h. (a), (b) Meridional; (c), (d) vertical; and (e), (f) zonal advection; (g) condensational heating. The shaded regions indicate the positive anomaly. The solid triangle indicates the low center defined by SLP.

by the strong convective heating and meridional warm air advection there (Figs. 14b and 14g), resulting in the positive anomaly of potential temperature (Fig. 13f). Near the low center, strong adiabatic warming dominates the other terms, showing that the warm core structure for experiment M3 is caused by the adiabatic

warming associated with the downdraft (see also Figs. 13d,f).

2) SENSITIVITY TO THE INITIAL PERTURBATION

To check the sensitivity of experiment M3 to the initial perturbation, we have performed three additional

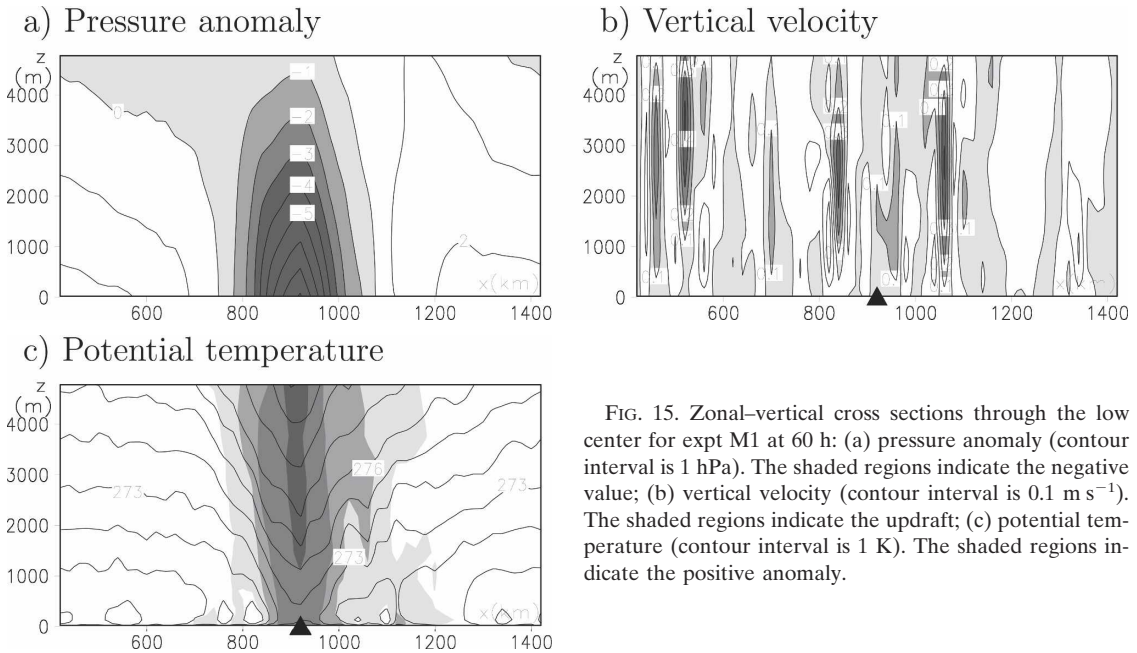


FIG. 15. Zonal–vertical cross sections through the low center for expt M1 at 60 h: (a) pressure anomaly (contour interval is 1 hPa). The shaded regions indicate the negative value; (b) vertical velocity (contour interval is 0.1 m s^{-1}). The shaded regions indicate the updraft; (c) potential temperature (contour interval is 1 K). The shaded regions indicate the positive anomaly.

experiments: in experiment M3-V2, a weak vortex with $V_{\max} = 2 \text{ m s}^{-1}$ is prescribed, while a large vortex with $r_{\max} = 50 \text{ km}$ is prescribed in M3-R50. (These settings of the initial vortex are similar to experiments M0-V2 and M0-R50 in section 3b.) In addition, we have also performed experiment M3-RDM in which a white noise of potential temperature having an amplitude of 0.5 K and random phases, instead of the initial vortex, are initially prescribed over the whole domain. Figure 10d shows the time evolution of the EKE for these experiments together with experiment M3. In contrast to similar experiments for the no baroclinicity case (section 3b), the growth rates of the EKE for all the experiments are nearly of the same magnitude except that the timing for the vortex development is different among the experiments. Figures 11d–f show horizontal distributions of the cloud pattern for experiments M3-R50 and M3-RDM at the development stage of the vortex. In all experiments (not shown for M3-V2), the cloud patterns eventually grow into a comma shape (Figs. 11d and 11f), similar to that realized in experiment M3 (Fig. 4f), although the cloud pattern at its initial stage for experiment M3-RDM (Fig. 11e) appears to indicate a wavenumber-2 disturbance with its wave front directed to the northwest–southeast direction. These results show that, when baroclinicity is large, the growth rate and morphology of the lows at their mature stage depend little on the initial disturbance.

d. Intermediate baroclinicity case (experiment M1)

In experiment M1, the strength of the basic baroclinicity is intermediate between those in M0 and M3.

Here, we will investigate the structures and dynamics of the vortex in experiment M1. We will also focus on the northward movement of the vortex, as seen in Fig. 5, and the sensitivity of the vortex development to initial perturbations.

1) STRUCTURE AND DYNAMICS

Figure 15 shows the zonal–vertical cross section of the pressure anomaly, vertical velocity, and potential temperature through the low center. The trough axis tilts little to the west with increasing height (Fig. 15a). Intense convection occurs within 150 km from the low center on both eastern and western sides (Fig. 15b) and extends to the height of 4 km ASL. At the low center, a warm core structure is remarkable (Fig. 15c). Most of the vortex characteristics for experiment M1 are thus similar to those for M0. However, the characteristic that the potential temperature is higher on the eastern side of the trough than on the western side (Fig. 15c) is similar to that in M3. Thus, the structure for experiment M1 is also intermediate between experiments M0 and M3.

2) NORTHWARD MOVEMENT

In section 3a, it was found that the vortex in experiment M1 moves northward in addition to the eastward advection by the basic zonal flow. To understand the mechanism for the northward movement, we have investigated the balance of terms in the vorticity equation averaged for the layer between 0 and 1 km ASL (Fig.

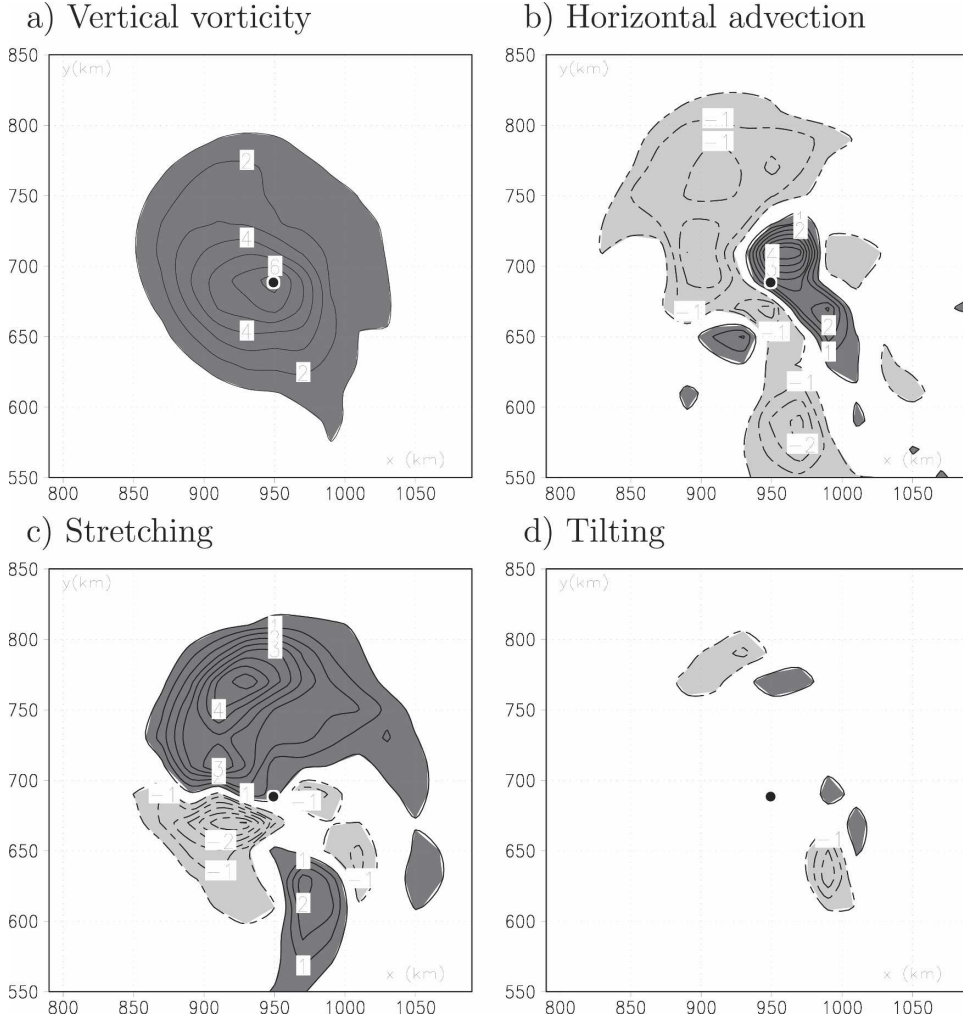


FIG. 16. Vertical vorticity and the terms in the equation of its budget between 0 and 1 km ASL and between 40 and 60 h for expt M1. Note that the horizontal location of the data is adjusted so that the low center is located at the same position through the average period: (a) vertical vorticity, (b) horizontal advection term, (c) stretching term, and (d) tilting term. Contour interval: $1 \times 10^{-4} \text{ s}^{-1}$ for (a) and $0.5 \times 10^{-8} \text{ s}^{-1}$ for (b)–(d). The zero contour line is omitted for clarity. The heavy (light) shading indicates positive (negative) value. The solid circle indicates the low center defined by SLP.

16). The horizontal advection simply moves the vortex eastward with a positive value on the eastern side of the vortex and negative on the west (Fig. 16b). The stretching term is positive on the northern side of the vortex and is dominant (Fig. 16c). The tilting term is much smaller than the other two terms (Fig. 16d). Since the movement of the vortex is determined by the location of the vorticity tendency (the sum of the advection, stretching, and tilting terms) relative to the vorticity maximum, it could be concluded that the stretching of the vorticity dominantly causes the northward propagation of the vortex in experiment M1.

The stretching of the vertical vorticity on the northern side of the vortex occurs due to convergence in the

lower layer of the active convection region there (Fig. 4i). To understand why the convection is active on the northern side of the vortex, we analyzed the horizontal advection of equivalent potential temperature in the lower atmosphere (Fig. 17). It is seen that high equivalent potential temperature occurs at the center and on the eastern side of the vortex. The cyclonic circulation, which transports the high equivalent potential temperature from the northeastern side of the vortex to the northwest, results in the large positive horizontal advection of equivalent potential temperature on the northern side of the vortex. This reduces the moist stability there and results in the active convection.

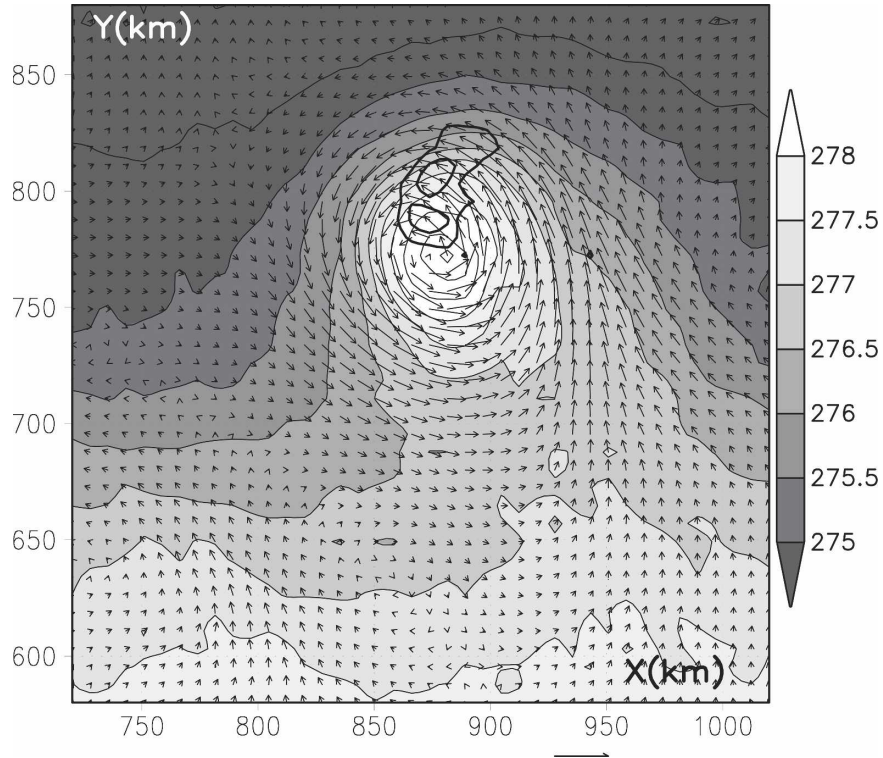


FIG. 17. Equivalent potential temperature (shading; K), its horizontal advection (contours are 0.2 and 0.4 K h^{-1}) and horizontal wind vector near the low center averaged between 0 and 1 km and between 40 and 60 h for expt M1. The horizontal location of the data is adjusted so that the low center is located at the same position through the average period.

3) SENSITIVITY TO THE INITIAL PERTURBATIONS

Finally, let us examine the sensitivity of experiment M1 to initial perturbations. The experiments M1-V2 (a weak initial vortex), M1-R50 (a large vortex), and M1-RDM (random noise of potential temperature) have been performed (see sections 3b, c for detailed explanation of the setting). Figure 10c shows the time evolution of the EKE for the three experiments together with that for experiment M1. As in experiment M3, the growth rate of the EKE for all experiments is nearly the same as that in M1, although the vortex in experiment M1-RDM seems to develop slightly slower than it does in the other experiments. Thus, the sensitivity to the initial perturbation for experiment M1 is intermediate between experiments M0 and M3.

4. Discussion

a. Dependence of vortex characteristics on baroclinicity

The results of the control experiments give us a comprehensive understanding of how the baroclinicity

of the basic state affects the structures and dynamics of the vortex. Within the range of typically observed baroclinicity, a variety of vortices can develop. The characteristics of the vortices are summarized in Table 1 for the representative experiments M0, M1, and M3.

In experiment M0, the cloud pattern shows the axisymmetry with a cloud-free eye at its center, which resembles a tropical cyclone. Polar lows with nearly axisymmetric cloud pattern and spiral cloud bands have been observed in satellite images (e.g., Businger and Baik 1991; Nordeng and Rasmussen 1992), although their basic baroclinicity were not shown. Note that the 2-km resolution corresponding to the simulation by YN05 also reproduced clear spiral bands around the eyewall. Similar to a tropical cyclone, the surface friction causes a strong inflow that transports angular momentum and water vapor toward the low center. At the low center, the downdraft (Fig. 8d) transports dry and high potential temperature air from the upper atmosphere, which causes the warm core (Fig. 8f) and the cloud-free eye (Fig. 8a). As in the axisymmetric experiment by Emanuel and Rotunno (1989), the vortex de-

TABLE 1. Characteristics of the vortices that develop in the environment with different baroclinicity. The arrows in the third column (expt M1) denote intermediate characteristics between expts M0 and M3.

Baroclinicity	Zero (M0)	Intermediate (M1)	Strong (M3)
Cloud pattern	Axisymmetric with cloud-free eye and spiral bands	Slightly nonaxisymmetric with convection on the north side	Comma shape with a cloud band on the east side
Horizontal scale	~300 km	↔	Larger than 500 km
Growth rate of EKE	Small	↔	Large
Time scale for the development	Longer than 70 h	↔	~30 h
Zonal movement	None	↔	Eastward
Meridional movement	None	Northward	None
$[P_m, P_e]/[Q, P_e]$	0	↔	~1
$[K_m, K_e]/[P_e, K_e]$	0	↔	~0.3
Sensitivity to surface friction	Strong	↔	Weak
Sensitivity to initial vortex	Strong	↔	Weak
Role of condensational heating	Essential for the development	↔	Increase the growth rate and modify the structure
Role of baroclinicity	None	↔	Essential for the development

development in experiment M0 significantly depends on the initial perturbation.

In experiment M3, the meso- α -scale structure of the vortex shows characteristics similar to that of the dry baroclinic instability wave: the trough axis tilts westward with increasing height and the updraft occurs within the region of warm air meridional advection to the east of the low center. Comparison between experiments M3 and D3 shows that the condensational heating increases the growth rate of the baroclinic wave (Fig. 3b) and decreases the horizontal scale (Fig. 12), consistent with the results of previous studies [e.g., Mak (1982) and Wang and Barcilon (1986) for a quasigeostrophic system; Emanuel et al. (1987) for a semigeostrophic system]. Wang and Barcilon showed that convective heating works more effectively for increasing the growth rate when the stratification is weaker and the heating occurs at lower altitude. This condition is satisfied in our experiment where the vertical gradient of potential temperature is 1 K km^{-1} and the maximum of condensational heating is at $\sim 2500 \text{ m ASL}$ (not shown). In addition, the effect of the condensational heating causes the meso- β -scale structure such as an updraft within a narrow convective band, an upright trough axis, and a warm core at the low center. Thus, the vortex for experiment M3 has a multiscale structure. The strong and narrow updraft (Fig. 13d) is consistent with the previous studies by Emanuel et al. (1987) and Fantini (1999) in which the condensational heating is parameterized. It should be also noted that the conversion from MKE (the basic vertical shear flow) to EKE (Fig. 6f) and the cloud pattern elongated in northwest-southeast direction for experiment M3-RDM (Fig. 11e) at 50 h are consistent with the nongeostrophic baroclinic dynamics studied by Yanase and Niino (2004). Since surface friction slightly weakens the

vortex development (Figs. 7a and 7b), the convection seems to be controlled by the updraft by baroclinic waves rather than Ekman pumping, which appears to correspond to the case of a deeper moist layer in Wang and Barcilon (1986). Polar lows with comma-shaped cloud patterns in relatively strong baroclinicity [$2 \sim 4 (\times 10^{-3} \text{ s}^{-1})$] have also been observed [e.g., Reed and Duncan (1987) and Shapiro et al. (1987); the baroclinicity for the latter is estimated in Craig and Cho (1988)]. A cloud-free center in a polar low that develops in strong baroclinicity has been observed by radar (Hewson et al. 2000; Fu et al. 2004) and simulated by a nonhydrostatic model (Yanase et al. 2002).

Most of the characteristics of the vortex vary smoothly with increasing the baroclinicity from experiments M0 to M4. In experiment M1, therefore, the vortex shows the intermediate characteristics between experiments M0 and M3 (Table 1). One of the unique characteristics of experiment M1, however, is that the vortex has intense convection on the northern side, which causes the northward movement of the vortex through the vortex stretching. Polar lows having weak asymmetry with intense convection on the northern side of the low center have been observed in intermediate baroclinicity [e.g., Rasmussen (1981) and Rasmussen (1985) whose baroclinicity are estimated by Sardie and Warner (1983) and Craig and Cho (1988), respectively].

b. Sensitivity to stratification and average temperature

In the previous sections, we have examined the dependence of vortex characteristics on baroclinicity for the control experiments, in which the vertical gradient of potential temperature is fixed to 1 K km^{-1} below 5 km ASL and the potential temperature at the surface is

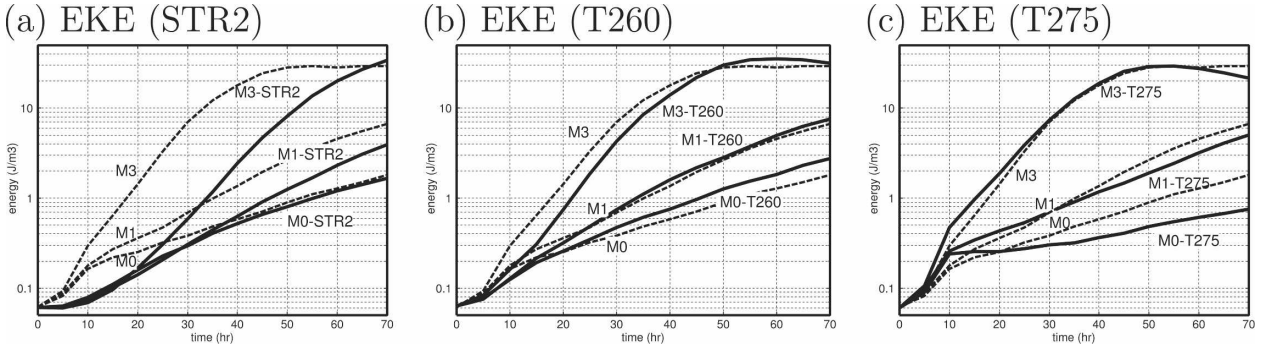


FIG. 18. Time evolutions of the EKE (solid lines) for (a) strong-stratification experiments, (b) low-temperature experiments, and (c) high-temperature experiments. Those for the control experiments (expts M0, M1, and M3) in Fig. 3 are also shown by dashed lines as references.

fixed to 270 K. In the real atmosphere, however, not only the baroclinicity but also the stratification and average temperature could vary from case to case. Therefore, we have performed three sets of additional experiments: 1) strong-stratification experiments in which the vertical gradient of potential temperature below 5 km ASL is increased to 2 K km^{-1} while keeping the potential temperature at the sea surface level the same as that in the control experiment (270 K); 2) low-temperature experiments in which both the entire atmospheric potential temperature and sea surface temperature are decreased by 10 K (260 K); and 3) high-temperature experiments, which are the same as the low-temperature experiments except that all the temperatures are increased by 5 K (275 K). The sensitivity experiments 1), 2), and 3) corresponding to experiment M0, for example, are referred to as experiments M0-STR2, M0-PT260, and M0-PT275, respectively.

Figure 18 shows the time evolution of EKE for the three sets of sensitivity experiments corresponding to M0, M1, and M3. In all experimental sets, the growth rate of EKE becomes large as the baroclinicity is increased, which is the same tendency as in the control experiments. In the strong-stratification experiments (Fig. 18a), the initial growth rates for experiments M0-STR2, M1-STR2, and M3-STR become much smaller than for the control experiment experiments M0, M1, and M3. After 20 h, when the surface heat fluxes weaken the initial stratification, however, the growth rates become nearly comparable to those in the control experiments. The growth rate for experiment M0-PT260 (Fig. 18b) is slightly larger than for experiment M0 and that for experiment M0-PT275 (Fig. 18c) is smaller than that for the latter. The cumulus convection for experiment M0-PT275 appears to be too active—not only near the vortex center but also over all of the calculation domain—to be organized into a vortex. The sensitivity of the vortex development to average tem-

perature becomes small as the baroclinicity is increased.

Figure 19 shows the horizontal distribution of cloud patterns at the development stage of the vortices in the sensitivity experiments shown in Fig. 18. The horizontal scale, cloud pattern, and meridional movement for all sets of additional experiments are similar to those for the control experiments summarized in Table 1. In the high-temperature experiments, however, cumulus convection is extremely active, not only near the vortex center but also over the whole domain.

The above results confirm that the general tendency of the growth rate, cloud pattern, and movement with increasing baroclinicity for the control experiments remain valid for the typically observed range of the vertical gradient of the basic potential temperature and of the average potential temperature.

5. Summary and conclusions

Our previous study (YN05) on the dependence of morphology of polar lows on environmental baroclinicity using a high-resolution nonhydrostatic model is extended to clarify their detailed structures, dynamics, and sensitivities to various physical processes.

The results are summarized as follows: for experiment M0 in which the basic state has no baroclinicity the vortex exhibits characteristics similar to those of a tropical cyclone: a warm core structure, a cloud-free eye, and an eyewall. Surface friction plays an important role to organize cumulus convection in the vortex through transport of water vapor and heat to the vortex center. The development of the vortex significantly depends on the initial perturbation. For experiment M3 with strong baroclinicity, the meso- α -scale structure of the vortex resembles that of an ordinary dry baroclinic instability wave. However, the vortex exhibits meso- β -

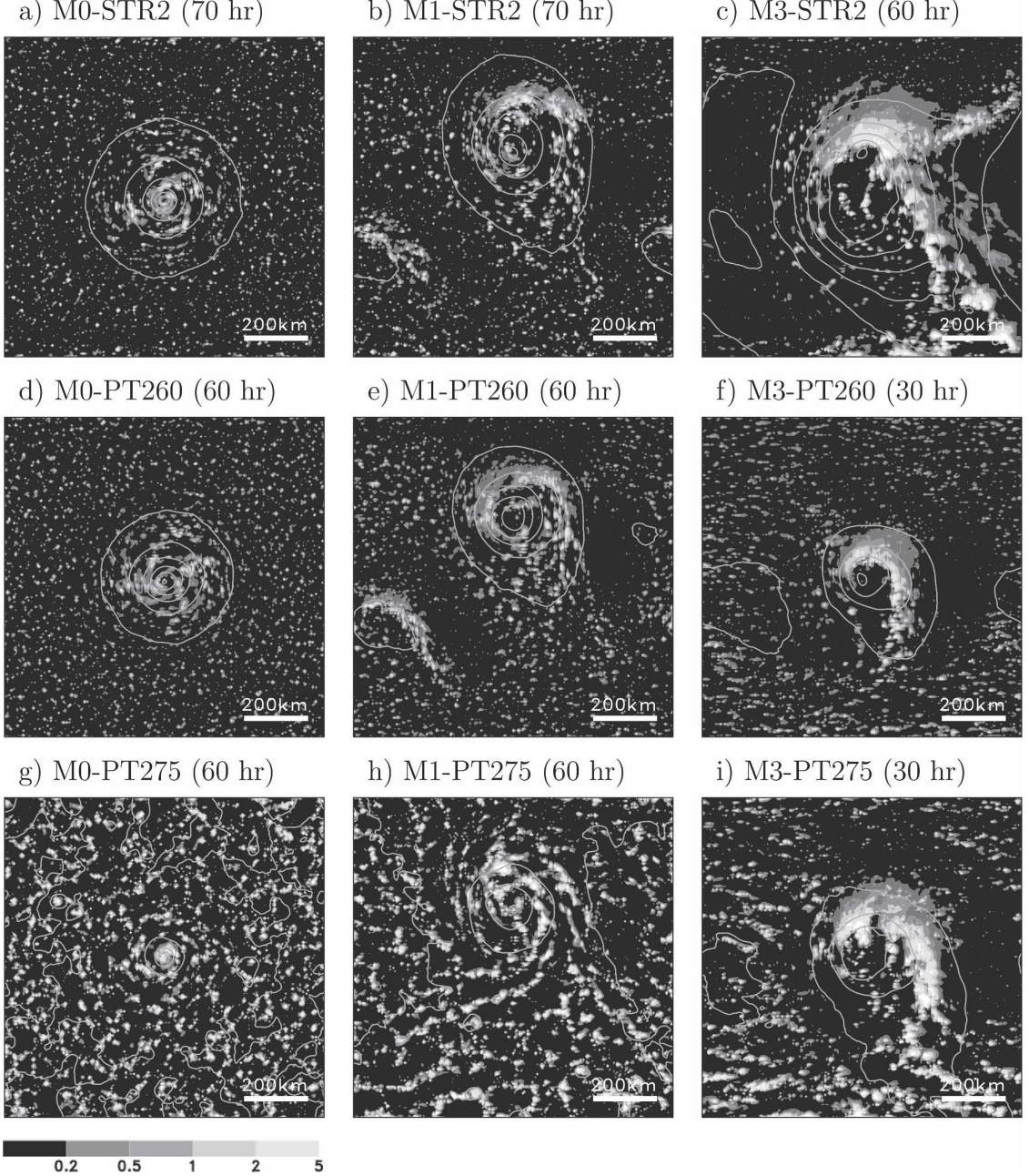


FIG. 19. Vertically integrated total condensed water (shade) and SLP (contour interval is 3 hPa) at their development stages for (a) M0-STR2 (70 h), (b) M1-STR2 (70 h), (c) M3-STR2 (60 h), (d) M0-PT260 (60 h), (e) M1-PT260 (60 h), (f) M3-PT260 (30 h), (g) M0-PT275 (60 h), (h) M1-PT275 (60 h), and (i) M3-PT275 (30 h).

scale structures caused by condensational heating: an updraft within the narrow convective band to the northern and eastern sides of the low center, the upright trough axis, and a warm core structure near the low center. The horizontal scale of the vortex is also considerably smaller than that for the dry baroclinic wave. The energy budget shows that, in addition to the generation of EKE from EPE, that from MKE (the vertical

shear of the mean zonal flow) is notable, which is characteristic of a nongeostrophic baroclinic instability (Yanase and Niino 2004). The initial disturbance is found to have little effect on the subsequent vortex development and structure for experiment M3. The characteristics of the low change smoothly with increasing baroclinicity (from experiment M0 to M4), demonstrating that no drastic regime shift or jump occurs at a particu-

lar baroclinicity. In fact, the vortex structure for experiment M1 shows that most of the vortex characteristics are intermediate between experiments M0 and M3. One of the unique characteristics of experiment M1, however, is that the vortex tends to move northward in addition to the eastward movement. This northward movement is caused by vorticity stretching due to a stronger updraft in the region of active cumulus convection on the northern side of the vortex. It should be noted that the relation between vortex characteristics and baroclinicity, as found for the control experiments (M0–M4), is robust within the observed range of the stratification and average temperature of the basic state.

One of the important contributions of the present idealized experiment is to suggest a unified picture among the observational and theoretical studies in the past: In the previous case studies using observational data and/or numerical simulations, so many factors could have affected the dynamics of polar lows, and it was not easy to understand with confidence which factor significantly determines the characteristics of the polar low. In the previous theoretical studies based on linear analysis, on the other hand, the physical processes such as cumulus convection are so simplified that it was not clear to what degree the vortex dynamics is reproduced realistically. In the present study, the design of the numerical experiment is simple enough to make the interpretation of the vortex dynamics easy while the representation of the vortex structure and organized convection is sufficiently realistic by using a three-dimensional nonhydrostatic model with horizontal resolution of 5 km.

The simplification of the problem, however, has been attained by neglecting several additional factors that could affect the dynamics of polar lows. These include interactions with the upper-level trough, effects of non-zero zonal flow at the sea surface level, the effects of baroclinicity that is confined to a finite meridional belt, and so on. The effects of these factors are to be studied in future work. In addition, although the Coriolis parameter in the present study is designed to be constant for the value at 70°N, polar lows in the real atmosphere are observed in the range from ~40°N (e.g., the Japan Sea) to 70°N (e.g., the Norwegian and Barents Seas). It is expected that the horizontal scale of polar lows would become larger at lower latitude, according to theoretical studies by Wang and Barcilon (1986) and Wang (1987). Since the thermal wind relation between the meridional gradient of temperature and vertical shear of zonal wind depends on the Coriolis parameter, the criterion for “strong” or “intermediate” baroclinicity could be modified at different latitudes. The sensitivity

of the dynamics to different values of a constant Coriolis parameter will also be examined in a future study. We believe that the present study provides an important basis for such future studies. This type of idealized experiment may be also useful for understanding rapidly intensifying extratropical cyclones (Kuo and Low-Nam 1990), or “meteorological bombs,” and extratropical transition of tropical cyclones (Jones et al. 2003) in which both condensational heating and baroclinic instability play important roles (e.g., Hart 2003).

Acknowledgments. The present simulations were done by using MRI/NPD-NHM on the IBM Regatta Parallel Computing System at the Ocean Research Institute, the University of Tokyo. This paper is a part of Wataru Yanase's Ph.D. thesis submitted to the Department of Earth and Planetary Physics, the University of Tokyo. The authors are grateful to Drs. Bin Wang and Fu Gang and an anonymous reviewer for constructing comments for improving the quality of the manuscript. WY was partly supported by a grant for the 21st Century COE Program “Predictability of the Evolution and Variation of the Multiscale Earth System: An Integrated COE for Observational and Computational Earth Science” from MEXT, and by Grant-in-Aids for Scientific Research (B) 18340137, Japan Society for the Promotion of Science.

REFERENCES

- Albright, M. D., and R. J. Reed, 1995: Origin and structure of a numerically simulated polar low over Hudson Bay. *Tellus*, **47A**, 834–848.
- Bratseth, A. M., 1985: A note on CISK in polar air masses. *Tellus*, **37A**, 403–406.
- Businger, S., and R. J. Reed, 1989: Cyclogenesis in cold air masses. *Wea. Forecasting*, **4**, 133–156.
- , and J.-J. Baik, 1991: An arctic hurricane over the Bering Sea. *Mon. Wea. Rev.*, **119**, 2293–2322.
- Carleton, A. M., 1985: Satellite climatological aspects of the “polar low” and “instant occlusion.” *Tellus*, **37A**, 433–450.
- Craig, G., and H. R. Cho, 1988: Cumulus heating CISK in the extratropical atmosphere Part I: Polar lows and comma clouds. *J. Atmos. Sci.*, **45**, 2622–2640.
- Deadorff, J. W., 1980: Stratocumulus-capped mixed layers derived from a three-dimensional model. *Bound.-Layer Meteor.*, **18**, 495–527.
- Duncan, C. N., 1977: A numerical investigation of polar lows. *Quart. J. Roy. Meteor. Soc.*, **103**, 255–267.
- Eady, E. T., 1949: Long waves and cyclone waves. *Tellus*, **1**, 33–52.
- Emanuel, K. A., and R. Rotunno, 1989: Polar lows as arctic hurricanes. *Tellus*, **41A**, 1–17.
- , M. Fantini, and A. J. Thorpe, 1987: Baroclinic instability in an environment of small stability to slantwise moist convection. Part I: Two-dimensional models. *J. Atmos. Sci.*, **44**, 1559–1573.
- Fantini, M., 1999: Linear evolution of baroclinic waves in saturated air. *Quart. J. Roy. Meteor. Soc.*, **125**, 905–923.

- Forbes, G. S., and W. D. Lottes, 1985: Classification of mesoscale vortices in polar airstreams and the influence of the large-scale environment on their evolutions. *Tellus*, **37A**, 132–155.
- Fu, G., H. Niino, R. Kimura, and T. Kato, 2004: A polar low over the Japan Sea on 21 January 1997. Part I: Observational analysis. *Mon. Wea. Rev.*, **132**, 793–814.
- Grönås, S., and N. G. Kvamstø, 1995: Numerical simulations of the synoptic conditions and development of Arctic outbreak polar lows. *Tellus*, **47A**, 797–814.
- Harley, D. G., 1960: Frontal contour analysis of a polar low. *Meteor. Mag.*, **89**, 146–147.
- Harrold, T. W., and K. A. Browning, 1969: The polar low as a baroclinic disturbance. *Quart. J. Roy. Meteor. Soc.*, **95**, 710–723.
- Hart, R. E., 2003: A cyclone phase space derived from thermal wind and thermal asymmetry. *Mon. Wea. Rev.*, **131**, 585–615.
- Heinemann, G., 1990: Mesoscale vortices in the Weddell Sea region (Antarctica). *Mon. Wea. Rev.*, **118**, 779–793.
- , and C. Claud, 1997: Report of a workshop on “theoretical and observational studies of polar lows” of the European Geophysical Society Polar Lows Working Group. *Bull. Amer. Meteor. Soc.*, **78**, 2643–2658.
- Hewson, T. D., G. C. Craig, and C. Claud, 2000: Evolution and mesoscale structure of a polar low outbreak. *Quart. J. Roy. Meteor. Soc.*, **126**, 1031–1063.
- Jones, S. C., and Coauthors, 2003: The extratropical transition of tropical cyclones: Forecast challenges, current understanding, and future directions. *Wea. Forecasting*, **18**, 1052–1092.
- Kondo, J., 1975: Air-sea bulk transfer coefficients in diabatic conditions. *Bound.-Layer Meteor.*, **9**, 91–112.
- Kuo, Y.-H., and S. Low-Nam, 1990: Prediction of nine explosive cyclones over the western Atlantic ocean with a regional model. *Mon. Wea. Rev.*, **118**, 3–25.
- Lee, T. Y., Y. Y. Park, and Y. L. Lin, 1998: A numerical modeling study of mesoscale cyclogenesis to the east of Korean Peninsula. *Mon. Wea. Rev.*, **126**, 2305–2329.
- Lin, Y. H., R. D. Farley, and H. D. Orville, 1983: Bulk parameterization of the snow field in a cloud model. *J. Climate Appl. Meteor.*, **22**, 1065–1092.
- Mak, M., 1982: On moist quasi-geostrophic baroclinic instability. *J. Atmos. Sci.*, **39**, 2028–2037.
- Mansfield, D. A., 1974: Polar lows: the development of baroclinic disturbances in cold air outbreaks. *Quart. J. Roy. Meteor. Soc.*, **100**, 541–554.
- Montgomery, M. T., and B. F. Farrell, 1992: Polar low dynamics. *J. Atmos. Sci.*, **49**, 2484–2505.
- Moore, G. W. K., and P. W. Vachon, 2002: A polar low over the Labrador Sea: Interactions with topography and an upper-level potential vorticity anomaly, and an observation by RADARSAT-1 SAR. *Geophys. Res. Lett.*, **29**, 1773, doi:10.1029/2001GL014007.
- Murakami, M., 1990: Numerical modeling of dynamical and microphysical evolution of an isolated convective cloud—The 19 July 1981 CCOPE cloud. *J. Meteor. Soc. Japan*, **68**, 107–128.
- Nordeng, T. E., and E. A. Rasmussen, 1992: A most beautiful polar low: A case study of a polar low development in the Bear Island region. *Tellus*, **44A**, 81–99.
- Økland, H., 1987: Heating by organized convection as a source of polar low intensification. *Tellus*, **39A**, 397–401.
- Orlanski, I., 1975: A rational subdivision of scales of atmospheric processes. *Bull. Amer. Meteor. Soc.*, **56**, 527–530.
- Pagowski, M., and G. W. K. Moore, 2001: A numerical study of an extreme cold-air outbreak over the Labrador Sea: Sea ice, air-sea interaction, and development of polar lows. *Mon. Wea. Rev.*, **129**, 47–72.
- Rasmussen, E., 1979: The polar low as an extratropical CISK disturbance. *Quart. J. Roy. Meteor. Soc.*, **105**, 531–549.
- , 1981: An investigation of a polar low with a spiral cloud structure. *J. Atmos. Sci.*, **38**, 1785–1792.
- , 1985: A case study of a polar low development over the Barents Sea. *Tellus*, **37A**, 407–418.
- , and J. Turner, Eds., 2003: *Polar Lows: Mesoscale Weather Systems in the Polar Regions*. Cambridge University Press, 612 pp.
- Reed, R. J., and C. N. Duncan, 1987: Baroclinic instability as a mechanism for the serial development of polar lows: A case study. *Tellus*, **39A**, 376–384.
- Saito, K., T. Kato, H. Eito, and C. Muroi, 2001: Documentation of the Meteorological Research Institute/Numerical Prediction Division unified nonhydrostatic model. Meteorological Research Institute Tech. Rep. 28, 238 pp.
- Sardie, J. M., and T. T. Warner, 1983: On the mechanism for the development of polar lows. *J. Atmos. Sci.*, **40**, 869–881.
- , and —, 1985: A numerical study of the development mechanism of polar lows. *Tellus*, **37A**, 460–477.
- Shapiro, M. A., L. S. Fedor, and T. Hampel, 1987: Research aircraft measurements of a polar low over the Norwegian Sea. *Tellus*, **39A**, 272–306.
- Tokioka, T., 1973: A stability study of medium-scale disturbances with inclusion of convective effects. *J. Meteor. Soc. Japan*, **51**, 1–10.
- Tsuboki, K., and G. Wakahama, 1992: Mesoscale cyclogenesis in winter monsoon air streams: Quasi-geostrophic baroclinic instability as a mechanism of the cyclogenesis off the west coast of Hokkaido Island, Japan. *J. Meteor. Soc. Japan*, **70**, 77–93.
- Wang, B., 1987: Another look at CISK in polar oceanic air masses. *Tellus*, **39A**, 179–186.
- , and A. Barcilon, 1986: Moist stability of a baroclinic zonal flow with conditionally unstable stratification. *J. Atmos. Sci.*, **43**, 705–719.
- Yanase, W., and H. Niino, 2004: Structure and energetics of non-geostrophic non-hydrostatic baroclinic instability wave with and without convective heating. *J. Meteor. Soc. Japan*, **82**, 1261–1279.
- , and —, 2005: Effects of baroclinicity on the cloud pattern and structure of polar lows: A high-resolution numerical experiment. *Geophys. Res. Lett.*, **32**, L02806, doi:10.1029/2004GL020469.
- , —, and K. Saito, 2002: High-resolution numerical simulation of a polar low. *Geophys. Res. Lett.*, **29**, 1658, doi:10.1029/2002GL014736.
- , G. Fu, H. Niino, and T. Kato, 2004: A polar low over the Japan Sea on 21 January 1997. Part II: A numerical study. *Mon. Wea. Rev.*, **132**, 1552–1574.